https://doi.org/10.5194/gmd-2024-72
Preprint. Discussion started: 29 April 2024

Geoscientific Model Development Discussions

ISOM 1.0: A fully mesoscale-resolving idealized Southern Ocean model and the diversity of multiscale eddy interactions

Jingwei Xie[1,2], Xi Wang[3], Hailong Liu[4], Pengfei Lin[1,2], Jiangfeng Yu[1,2], and Zipeng Yu[1]

[1]State Key Laboratory of Numerical Modeling for Atmospheric Sciences and Geophysical Fluid Dynamics (LASG), Institute of Atmospheric Physics, Chinese Academy of Sciences, Beijing, China
[2]College of Earth and Planetary Sciences, University of Chinese Academy of Sciences, Beijing, China
[3]Beijing Institute of Radio Measurement, China Aerospace Science and Industry Corporation, Beijing, China
[4]Center for Ocean Mega-Science, Chinese Academy of Sciences, Qingdao, China

Correspondence: Jingwei Xie (xiejw23@mail3.sysu.edu.cn) and Hailong Liu (hlliu2@qnlm.ac)

Abstract. We describe an idealized Southern Ocean model (ISOM 1.0) that contains simplified iconic topographic features in the Southern Ocean and conduct a fully mesoscale-resolving (2 km) simulation based on the Massachusetts Institute of Technology general circulation model (MITgcm). The model obtains a fully developed and vigorous mesoscale eddying field with a k^{-3} eddy kinetic energy (EKE) spectrum and captures the topographic effect on stratification and large-scale flow. To make a more naturally conceptual introduction of large eddy simulation (LES) methods into ocean mesoscale parameterization, we propose the concept of mesoscale ocean direct numerical simulation (MODNS). A qualified MODNS dataset should resolve the first baroclinic deformation radius and ensure that the affected scales by the dissipation schemes are sufficiently smaller than the radius. Such datasets can serve as the benchmark for a priori and a posteriori tests of LES schemes or mesoscale ocean large eddy simulation (MOLES) methods into ocean general circulation models (OGCMs). The 2 km idealized simulation meets the requirement of MODNS and also captures part of the submesoscale processes. Therefore, its output can be a type of MODNS and provide reliable data support for relevant a priori and a posteriori tests. We also illustrate the diversity and high complexity of multiscale eddy interactions related to mesoscale processes. We emphasize the importance of submesoscale phenomena on the evolution of mesoscale processes when mesoscale activities are vigorous and of high eddy number density. In addition, we use the model to conduct multipassive tracer experiments and reveal guidelines for the initial settings of passive tracers to delay the homogenization process and ensure the mutual independence of tracers over a long period.

1 Introduction

Oceanic mesoscale processes have motions with spatial scales of O(10km)-O(100km) or near the baroclinic Rossby deformation radius, including quasi-geostrophic eddies and meandering jets (Chelton et al., 1998; Hallberg, 2013; Siedler et al., 2013; Thompson and Naveira-Garabato, 2014; Youngs et al., 2017). These processes encompass more than 80% of the oceanic ki-

https://doi.org/10.5194/gmd-2024-72
Preprint. Discussion started: 29 April 2024

netic energy and play a crucial role in material transport, heat transport, momentum budget, and air-sea interactions. They also modulate climate variability across multiple timescales and engage in drastic multiscale interactions with both large-scale and submesoscale processes (Stammer, 1998; Ferrari and Wunsch, 2009; Zhai et al., 2010; Chelton et al., 2011; Dong et al., 2014; Ma et al., 2016; Vallis, 2017; Busecke and Abernathey, 2019; Schubert et al., 2020; Taylor and Thompson, 2023). Fully resolving oceanic processes at the mesoscale requires ocean general circulation models (OGCMs) with kilometer-scale horizontal resolution (Marques et al., 2022). Such models require massive computational and storage resources for long-term integration or large-ensemble experiments. Therefore, we still need parameterizations that capture the collective effects of the unresolved parts related to oceanic mesoscale processes in lower-resolution OGCMs.

The classic works on parameterizing oceanic mesoscale processes include the isoneutral diffusion scheme by Redi (1982) and the revolutionary Gent-McWilliams (GM) scheme (Gent and McWilliams, 1990; Gent et al., 1995) that represents the effect of eddy-induced adiabatic advection as well as generates a net sink of available potential energy. These two schemes are widely used in coarse-resolution OGCMs and can be represented by a flux-gradient relationship with an asymmetric transport tensor (Griffies et al., 1998). Since its inception, scholars have made considerable advancements in the field based on the GM-Redi framework. Additional specific constraints or properties, such as the stratification state (Visbeck et al., 1997), anisotropy (Smith and Gent, 2004), geometrical information (Mak et al., 2018), and energetic constraints (Cessi, 2007; Jansen and Held, 2014; Mak et al., 2018; Bachman, 2019; Jansen et al., 2019), have been embedded in the scheme to produce spatiotemporal variations in the transport coefficients.

In addition to the traditional theory-driven schemes described above, other studies have revealed the potential of large eddy simulation (LES) methods in oceanic mesoscale parameterization (Fox-Kemper and Menemenlis, 2008; Graham and Ringler, 2013; Pearson et al., 2017; Khani et al., 2019; Khani and Dawson, 2023; Xie et al., 2023; Perezhogin and Glazunov, 2023). The application is sometimes called the mesoscale ocean large eddy simulation (MOLES) (Fox-Kemper and Menemenlis, 2008; Graham and Ringler, 2013). First, one advantage of LES is in addressing the Reynolds averaging issue (Khani and Dawson, 2023; Xie et al., 2023; Perezhogin and Glazunov, 2023). Many parameterizations and related diagnostics originating from the GM-Redi framework are based on Reynolds averaging, which may simplify the derivation. However, the Reynolds averaging method inherently suppresses cross-scale interactions near the grid scale, leading to a loss of local information, and its mathematical properties are not fully satisfied by the grid discretization of numerical models (Leonard, 1974; Germano et al., 1991; Germano, 1992; Pope, 2000; Xie et al., 2023). Using Reynolds averaging as a grid discretization approximation in very coarse-resolution OGCMs might not cause significant issues. However, as the horizontal resolution of OGCMs increases, mesoscale or even submesoscale dynamics with multiscale interactions enter the model grid-scale regime, and local features should be considered when parameterizing subgrid-scale effects. Within the LES framework, subgrid-scale stress and flux terms that include local interactions can be fully expressed, thereby improving the simulation results. Second, the LES framework can also explicitly involve the stationary eddying effect as a supplement to traditional schemes that mainly focus on the transient eddying effect related to instabilities (Khani and Dawson, 2023; Xie et al., 2023). In addition, constructing parameterization schemes that combine LES with machine learning has become a frontier field in developing OGCMs (Bolton and Zanna, 2019; Zanna and Bolton, 2020; Guillaumin and Zanna, 2021; Frezat et al., 2022).

https://doi.org/10.5194/gmd-2024-72
Preprint. Discussion started: 29 April 2024

There are two types of tests for examining the performance of LES models (i.e. parameterization schemes in oceanography): a priori and a posteriori tests (Meneveau, 1994; Moser et al., 2021). In an a priori test, direct numerical simulation (DNS) for a specific flow is required first. Then, we perform the scale separation of DNS data through coarse-graining methods (e.g., spatial filtering). We regard the filtered field as an approximation of the coarser-resolution model output, and we directly diagnose the "true" subgrid-scale terms following their definition. Finally, we reconstruct the subgrid-scale terms by substituting the filtered field into the LES model. By investigating the performance of the reconstructed and the "true" subgrid-scale terms under given metrics (e.g., spatial correlations and the energy transfer rate), we can find out the properties of the LES model or parameterization scheme. In an a posteriori test, we embed the given LES scheme into a lower-resolution numerical model, run simulations, and test parameter sensitivity if needed. At this point, the macroscopic features of the corresponding flow from DNS data serve as the benchmark for evaluating the lower-resolution simulation results when applying the LES model. For both a priori and a posteriori tests, DNS data for the studied flow are essential. Therefore, when introducing LES methods into ocean mesoscale parameterization, it is necessary to generate DNS datasets for mesoscale processes, thereby facilitating the systematic work of developing, testing, and implementing any LES schemes into OGCMs.

In the literature of computational fluid dynamics, DNS requires the numerical model resolution to be at least close to the Kolmogorov scale (Moin and Mahesh, 1998; Pope, 2000; Kaneda and Ishihara, 2006; Alfonsi, 2011). It is the scale at which molecular viscosity becomes important (Pope, 2000; Vallis, 2017). However, the classical definition of DNS is inapplicable in the context of implementing LES methods into OGCMs. Carrying out simulations with resolution close to the Kolmogorov scale in OGCMs is not feasible in the foreseeable future, and it is also unnecessary to adopt such high resolution for merely simulating mesoscale motions. For oceanic mesoscale flow, the dynamically indicative scale is the first baroclinic deformation radius. The radius is in the range of approximately $10 \sim 40$ km in mid-latitude oceans (e.g., the Southern Ocean) (Chelton et al., 1998; LaCasce and Groeskamp, 2020), necessitating a horizontal resolution of at least $1/30°$ to resolve it explicitly (Hallberg, 2013; Marques et al., 2022). In addition, OGCMs often adopt dissipation schemes near the grid scale to ensure numerical stability. If the scale at which the dissipation scheme plays a significant role cannot be well separated from the first baroclinic deformation radius, then the intrinsic mesoscale dynamics would be contaminated artificially. Some works (e.g., Graham and Ringler, 2013; Radko and Kamenkovich, 2017) use the term DNS in the context of ocean mesoscale dynamics, which might lead to misunderstandings. Therefore, we hereby explicitly propose the concept of mesoscale ocean direct numerical simulation (MODNS). A qualified MODNS dataset not only requires the model grid to explicitly resolve the first baroclinic deformation radius but also demands that the affected scales by the dissipation scheme employed significantly smaller than the radius, making it the benchmark for a priori and a posteriori tests of LES schemes (or more specifically, MOLES methods) into OGCMs.

To highlight the oceanic mesoscale dynamics in the simulation while reducing computational and storage costs, we develop an idealized Southern Ocean model (ISOM 1.0) and conduct fully eddy-resolving experiments to generate a type of MODNS dataset. We emphasize that the focus of the simulations should be on controlling the dynamics of the idealized model rather than on precise comparisons with observations or realistic model results. We hope that the model can describe processes most closely associated with the mesoscale in the Southern Ocean, including mesoscale motions (mesoscale eddies and meandering

https://doi.org/10.5194/gmd-2024-72
Preprint. Discussion started: 29 April 2024

Geoscientific Model Development Discussions

jets), large-scale background processes (stratification and eastward transport similar to that in the realistic Southern Ocean), eddy-eddy interactions, eddy-jet interactions, large-scale topographic effects, and mesoscale-submesoscale interactions. ISOM enables us to achieve a MODNS in an idealized Southern Ocean with topography, thereby providing reliable supporting data for the design, testing, and application of any potential LES-related mesoscale parameterization schemes and the theoretical exploration of the dynamics.

We introduce the design philosophy and implementation methods of ISOM 1.0. We verify that the oceanic mesoscale regime is fully resolved and barely contaminated in the high-resolution simulation. In particular, we provide several vivid examples of multiscale eddy-eddy (or eddy-jet) interactions. These examples demonstrate that the high-resolution ISOM not only fully resolves the deformation radius but also explicitly captures a portion of the direct effects of submesoscale processes on mesoscale entities. Therefore, the simulation can serve as a type of MODNS dataset with vigorous eddy kinetic energy (EKE) and a high eddy number density. In addition, we conduct multipassive tracer experiments and explore the principles for setting the initial field combinations of passive tracers to offer technical references for relevant works.

2 Model description

2.1 Model equations and configurations

We establish ISOM 1.0 using the Massachusetts Institute of Technology general circulation model (MITgcm; Marshall et al., 1997). We refer to and improve upon the case of Southern Ocean Reentrant Channel Example in the MITgcm manual (Adcroft et al., 2024) that is closest to our needs, as well as similar idealized works (e.g., Abernathey et al., 2011; Bischoff and Thompson, 2014), ultimately achieving ISOM 1.0 with moderate complexity and topography. Similar to these works, we consider a hydrostatic, incompressible Boussinesq fluid on the β-plane, with an implicitly linearized free surface and a linearized equation of state (only potential temperature, no salinity). We employ the Cartesian coordinate, and then the governing equations are as follows:

$$\frac{Du}{Dt} - fv + \frac{1}{\rho_c}\frac{\partial p'}{\partial x} + \nabla_h \cdot (-A_h \nabla_h u) + \frac{\partial}{\partial z}\left(-A_z \frac{\partial u}{\partial z}\right) = \mathcal{F}_u, \tag{1}$$

$$\frac{Dv}{Dt} + fu + \frac{1}{\rho_c}\frac{\partial p'}{\partial y} + \nabla_h \cdot (-A_h \nabla_h v) + \frac{\partial}{\partial z}\left(-A_z \frac{\partial v}{\partial z}\right) = \mathcal{F}_v, \tag{2}$$

$$\frac{\partial \eta}{\partial t} + \nabla_h \cdot (H\widehat{\boldsymbol{u}}) = 0, \tag{3}$$

$$\frac{D\theta}{Dt} + \nabla_h \cdot (-\kappa_h \nabla_h \theta) + \frac{\partial}{\partial z}\left(-\kappa_z \frac{\partial \theta}{\partial z}\right) = \mathcal{F}_\theta, \tag{4}$$

https://doi.org/10.5194/gmd-2024-72
Preprint. Discussion started: 29 April 2024

Geoscientific Model Development Discussions
Open Access EGU

$$p' = g\rho_c\eta + \int_z^0 g\rho' dz. \tag{5}$$

The forcing terms of the horizontal momentum equation $\mathcal{F}_u$ and $\mathcal{F}_v$ include the steady zonal surface wind stress and the quadratic bottom drag. The wind stress is set as follows:

$$\tau_s(y) = \tau_0 \sin(\pi y/L_y), \tag{6}$$

with $\tau_0 = 0.2Nm^{-2}$. The dimensionless coefficient of quadratic bottom drag $C_d = 0.01$.

The forcing term of the potential temperature equation $\mathcal{F}_\theta$ includes relaxation to a prescribed surface temperature profile and a sponge layer at the northern side of the domain. The specified sea surface temperature profile increases linearly from 0°C in the south to 16°C in the north, with a relaxation time scale of 30 days (except in the sponge layer region). The sponge layer, or a three-dimensional subdomain where restoring boundary conditions are applied, is confined within 240 km at the northern side of the domain, and the potential temperature is relaxed to the following profile:

$$T(y,z) = [T_s(y) - T_b]\left(e^{-z/h_0} - e^{H/h_0}\right) / \left(1 - e^{H/h_0}\right). \tag{7}$$

T_s is the prescribed surface temperature profile that varies linearly and meridionally, T_b is the bottom temperature set to 0°C, the depth of the domain H is 3000 m, and the scaling height h_0 is taken as 1000 m (note that the z-coordinate origin is set at the surface). The setup can well represent the stratification on the northern side of the Antarctic Circumpolar Current (ACC; Abernathey et al., 2011). The relaxation time scale within 80 km at the northernmost part of the sponge layer is set to 7 days, that from 80 to 160 km is 14 days, and that from 160 to 240 km is 28 days. Tables 1 and 2 provide the settings for the other parameters of the governing equations.

2.2 Model bathymetry

The computational domain is a 14400 km × 2400 km channel with a prescribed topography and zonal periodic boundary conditions (Fig. 1). The domain depth is 3000 m, with 40 vertical levels, and the vertical grid spacing increases from 5 m at the surface to 200 m at the bottom. The channel mimics the hemispheric Southern Ocean that spans from the west of the Drake Passage to the east of the Kerguelen Plateau. This region has a highly complex topography and contains most of the iconic bathymetric features of the Southern Ocean. These features exert profound impacts on the holistic Southern Ocean flow. Using these iconic features enables the idealized model to preserve the complicated topographic effects on oceanic mesoscale processes. Although we could fill the entire domain with realistic topography, it would cause the bathymetric features to be too close to each other and excessively suppress the development of flow. Moreover, reducing computational and storage costs is another reason for imitating only half rather than the entire Southern Ocean.

We integrate four types of topography in the domain (Fig. 1). They are described in detail as follows.

(1) The first type is an idealized Drake Passage that is a passage from x = 800 km to x = 2800 km. It smoothly narrows from the sides to form a 1200 km × 600 km rectangular subchannel. The southeast, southwest, and northwest parts of the passage

Geoscientific Model Development
Discussions

Table 1. Basic parameters of the idealized Southern Ocean simulation.

Symbol	Value	Description
L_x, L_y	14400 km,2400 km	Domain size
H	3000 m	Domain depth
Δz	5 - 200 m	Vertical grid spacing
L_{sponge}	240 km	Sponge layer size
τ_{sponge}	7 days	Shortest Sponge layer relaxation time scale
λ	30 days	Surface temperature relaxation time scale (outside the sponge layer)
f_0	$-1 \times 10^{-4}\mathrm{s}^{-1}$	Reference Coriolis parameter
β	$1 \times 10^{-11}\mathrm{m}^{-1}\mathrm{s}^{-1}$	Meridional gradient of Coriolis parameter
g	9.81 m s^{-2}	gravitational acceleration
τ_0	0.2 N m^{-2}	Wind stress magnitude
C_d	1×10^{-2}	Quadratic bottom drag parameter
ρ_c	1035 kg m^{-3}	Reference density
α	$2 \times 10^{-4}\mathrm{K}^{-1}$	Linear thermal expansion coefficient
κ_v	5×10^{-6} m s^{-2}	Vertical diffusivity
κ_h	0	Horizontal diffusivity
A_v	3×10^{-4} m s^{-2}	Vertical viscosity

Table 2. Parameters of simulations with different horizontal resolution at their statistical steady state. DST-33 is 3rd order DST (direct space-time) flux limiter. 7-order is 7th order monotonicity-preserving scheme.

Symbol	Value-1	Value-2	Value-3	Description
$\Delta x, \Delta y$	2 km	4 km	8 km	Horizontal grid spacing
A_h	2	4	50	Horizontal viscosity(m s^{-2})
A_4	1×10^{8}	5×10^{9}	1×10^{10}	Horizontal hyperviscosity(m^4 s^{-1})
	DST-33	DST-33	7-order	Advection scheme
	33	33	7	MITgcm scheme code

are 1/4 circular arcs with a radius of 400 km. We use a cubic function to smoothly link the northeast part of the subchannel to the point (x, y) = (2800 km, 2400 km). The topography within the passage has a piecewise linear depth. The bottom rises from -3000 m to -2000 m within the range of x = 800 km to x = 1200 km. It ascends from -2000 m to -1000 m within the range of x

https://doi.org/10.5194/gmd-2024-72
Preprint. Discussion started: 29 April 2024

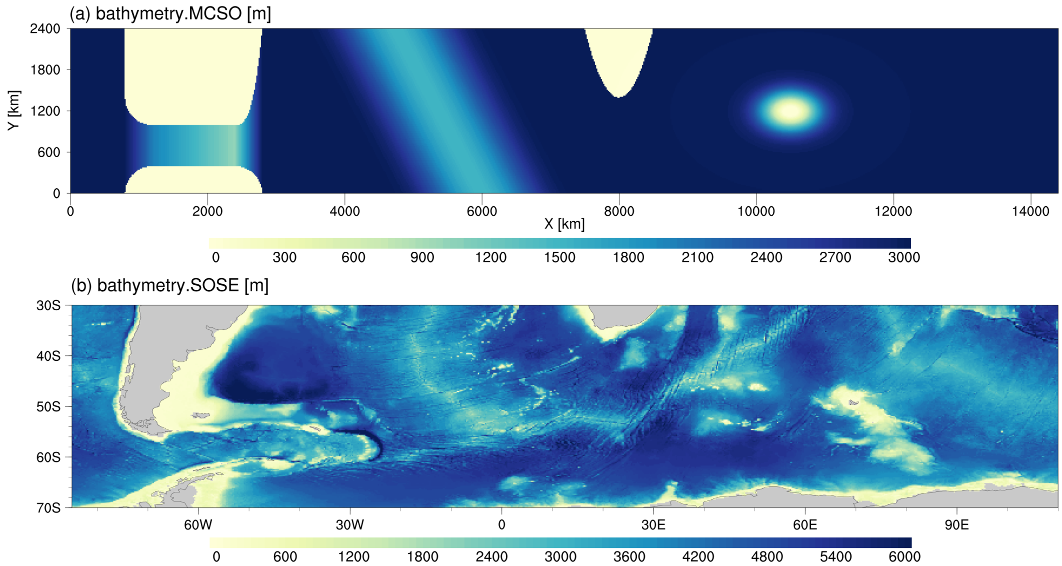

Figure 1. The bathymetry of (a) ISOM 1.0 and (b) Southern Ocean State Estimate (SOSE; Mazloff et al., 2010; Verdy and Mazloff, 2017)

= 1200 km to x = 2400 km. It descends from -1000 m to -3000 m within the range of x = 2400 km to x = 2800 km. Although the topography is highly simplified, it still helps the idealized model qualitatively reproduce the flow characteristics near the realistic Drake Passage (Fig. 2). We also tested the passage with a flat bottom and the semicircular ridge of the Neverworld-2 model, as mentioned in Marques et al. (2022). The idealized Drake Passage can generate a highly active (to some extent, overactive) eddy field, and the flat-bottom or semicircular ridge somehow suppresses eddy activity near the passage.

(2) The second type is an idealized mid-ocean ridge with zonal and meridional slopes. We have set up a tilted ridge downstream of the idealized Drake Passage with a zonal width w = 2500 km and height h_1 = 1500 m. The ridge is confined within a parallelogram with vertices at (x, y) = (3500 km, 2400 km), (6000 km, 2400 km), (4750 km, 0), and (7250 km, 0). In the x-z cross-section, the ridge is composed of piecewise cubic functions with height h expressed as follows:

$$h(x) = \begin{cases} -\frac{16h_1}{w^3}x^3 - \frac{12h_1}{w^2}x^2 + h_1, & -\frac{w}{2} < x < 0, \\ \frac{16h_1}{w^3}x^3 - \frac{12h_1}{w^2}x^2 + h_1, & 0 < x < \frac{w}{2}. \end{cases} \tag{8}$$

(3) The third type is an idealized African continent. We define a topography resembling the southern African continent with a quadratic function $y(x) = \frac{1}{250}(x - x_0)^2 + y_0$ and the vertex $(x_0, y_0) = (8000km, 1400km)$.

(4) The fourth type is an idealized Kergulen Plateau. We set a large-scale elliptical Gaussian plateau centered on (x_m, y_m) = (10500 km, 1200 km), and its height h is expressed as follows:

$$h(x,y) = h_2 \exp\left[-\frac{(x - x_m)^2}{2\sigma_x^2} - \frac{(y - y_m)^2}{2\sigma_y^2}\right]. \tag{9}$$

σ_x is taken as 300 km, σ_y is 200 km, and h_2 is 3200 m. Since h_2 > H = 3000 m, the plateau is above sea level in the expression. Thus, it is an elliptical landmass at the sea surface in the numerical model.

https://doi.org/10.5194/gmd-2024-72
Preprint. Discussion started: 29 April 2024

Geoscientific Model Development
Discussions
Open Access
EGU

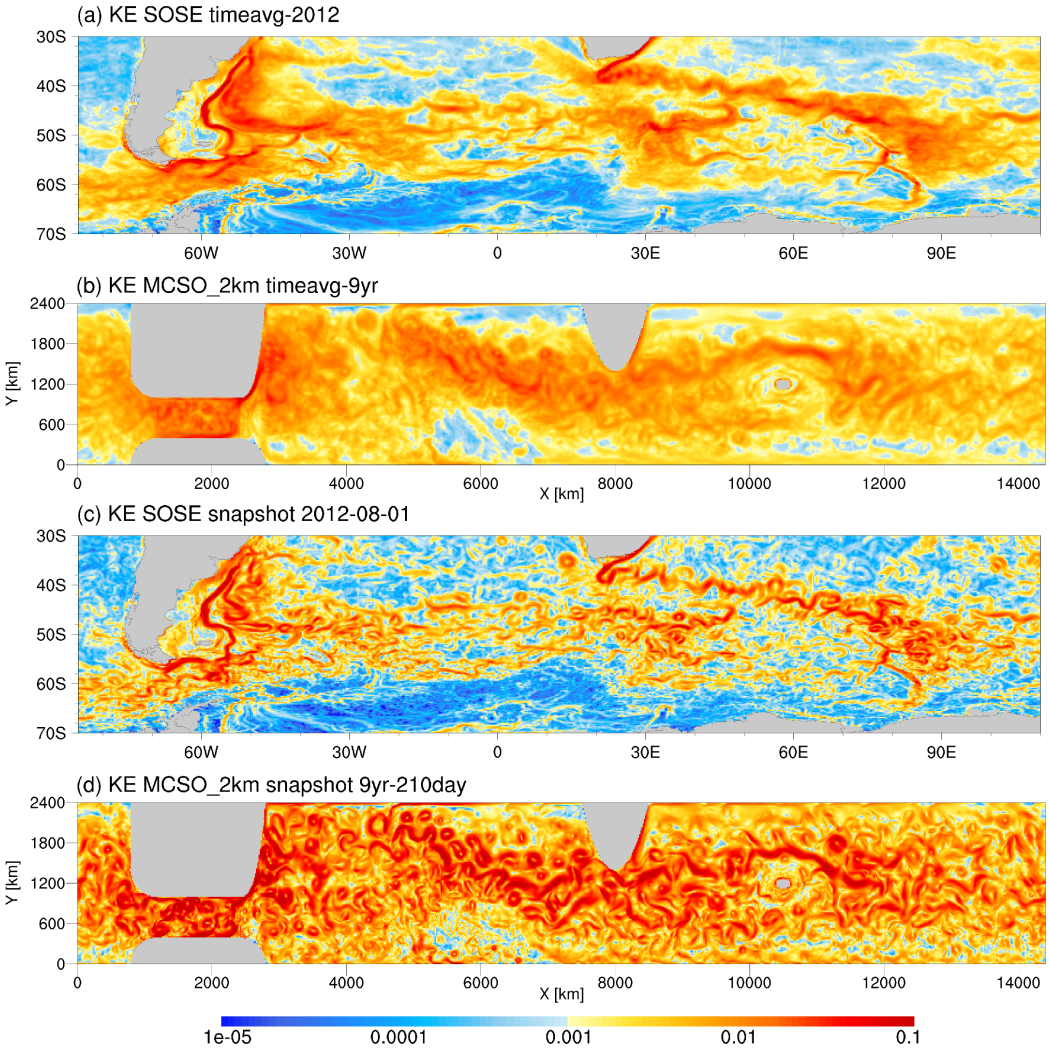

Figure 2. (a) The kinetic energy of time-averaged velocity in 2012 of SOSE, (b) the kinetic energy of time-averaged velocity in the 9th model year of the 2km idealized simulation, and the snapshot of kinetic energy of (c) SOSE and (d) the 2km simulation.

Although the topography in the model is highly idealized, the simulation qualitatively reproduces the major flow characteristics of the Southern Ocean (Fig. 2), such as intense eddy activity, enhanced currents downstream of large-scale topographic features, and the eastward extension of the current from southern Africa. By observing the differences between the simulated results and the realistic Southern Ocean and referring to other relevant works, we can gain experience and lessons for optimizing the model. We share the following insights:

(1) The highlight of the idealized model lies in the successful simulation of energetic mesoscale and submesoscale phenomena and the vivid depiction of multiscale eddy-eddy and eddy-jet interactions (see Section 3). However, large-scale processes in

https://doi.org/10.5194/gmd-2024-72
Preprint. Discussion started: 29 April 2024

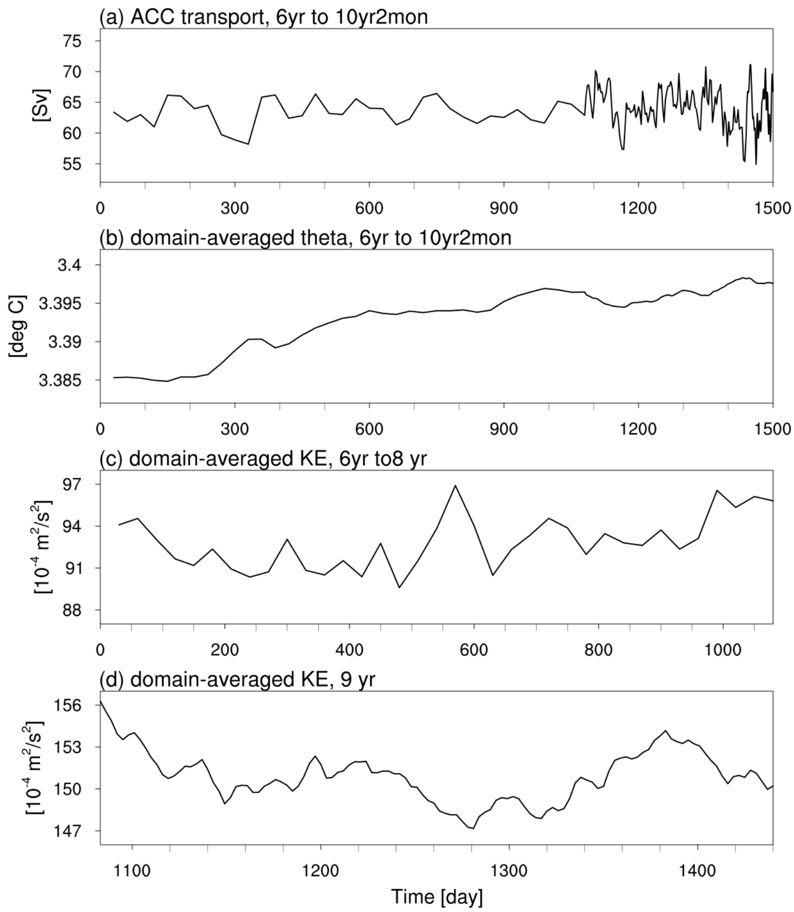

Figure 3. (a) The ACC transport from the 6th year to the first two months of the 10th year of the 2km simulation, with monthly averages in the first three years, 3-day averages in the fourth year, and daily snapshots in the last two months. (b) Domain-averaged potential temperature and (c)(d) Domain-averaged kinetic energy for the 2km simulation.

the simulation are under-developed. For example, the eastward transport of the ACC is underestimated compared with that in the realistic situation (Fig. 3a). Different observations and simulations (e.g., Cunningham et al., 2003; Park et al., 2009; Donohue et al., 2016; Xu et al., 2020; Artana et al., 2021a) yield varying values for ACC transport, but generally, they fall within the range of 130 to 180 Sv, which is also consistent with our calculation using Southern Ocean State Estimate (SOSE). The ACC transport in the idealized simulation is significantly lower than this range (approximately 65 Sv). Although we might attribute the deficiency to the highly idealized nature, the degree of this underestimation is still surprising. In contrast to our result, Neverworld-2 in Marques et al. (2022), whose domain contains an Atlantic-like cross-equatorial basin and a re-entrant channel in the South, simulates much stronger ACC transport (approximately 240 Sv) than that in the realistic situation. Their model enables the development of complete large-scale gyres and meridional overturning circulation, which may help enhance

https://doi.org/10.5194/gmd-2024-72
Preprint. Discussion started: 29 April 2024

eastward transport in the Southern Ocean. Due to the sponge layer at the northern boundary, our model insufficiently expresses large-scale processes (especially gyres), thereby hindering the buildup of ACC transport. In addition, the simulated eddies are very active and have a dense spatial distribution. Thus, the flow field has intense meridional displacement and a high degree of disorder, potentially blocking the ACC from developing consistent eastward transport (e.g., eddy traffic jam in the idealized Drake Passage, Fig. 2d). Although the ACC transport can be enhanced immediately under fixed wind stress by reducin bottom frictional drag, in practice, we find that it has the side effects of producing unreasonably large velocity at deep levels and further accelerating eddy velocity. Since the major purpose of the idealized simulation is to generate a MODNS dataset for the a priori and a posteriori tests of LES models and relevant parameterization design, we prefer to ensure that the eddying features vary only slightly from realistic ocean conditions. The side effects of adjusting the bottom drag coefficient would undoubtedly violate our intention. Given that we have achieved the major goal, that is, successfully resolving mesoscale processes, we decide to accept the weak simulated ACC and not to be concerned about the issue at this stage.

(2) Other idealized models of similar complexity, such as Neverworld in Khani et al. (2019) and Neverworld-2 in Marques et al. (2022), often apply a steep slope transition from the landmass to the domain depth to mimic the continental shelf. However, we find in tests that this leads to the formation of extremely strong currents driven by the topographic β effect near the side boundaries. Unfortunately, these currents interfere with the simulation of other processes in our idealized model. Marques et al. (2022) mentioned their application of significant lateral dissipation. This might be a way to weaken the overly abundant boundary currents. However, the major goal of our simulation is to obtain MODNS dataset. To avoid directly contaminating mesoscale dynamics, we are not inclined to use excessive viscous dissipation in fully eddy-resolving simulations. Therefore, we set the side boundaries to be vertical, which weakens the boundary flow and encourages a more eddying field.

(3) The highly complicated topography near the South American continent exerts a decisive influence on the surrounding flow, especially the presence of the Malvinas Islands shelf, which leads to a narrow and extensive boundary current (Artana et al., 2021b). ISOM 1.0 prioritizes the imitation of the Drake Passage and overly intensifies the eddy activity within the passage. If researchers conduct similar works in the future, we suggest weakening the bottom slope within the Drake Passage as well as optimizing the topographical expression along the South American continent.

(4) Previous studies (e.g., Speich et al., 2006; Lutjeharms and Van Ballegooyen, 1984; Lutjeharms, 2007) have shown that the topography near the Agulhas Retroflection region, such as the Agulhas Bank (the continental shelf extending southwest from the African continent) and the Agulhas Plateau (a large-scale seamount offshore to southeastern Africa), plays a crucial role in controlling the flow state of eddies and jets. Altering topographic features, such as the slope of the continental shelf and the degree of topographic undulations, substantially influences the flow path, eddy-shedding process, and cross-basin transport. ISOM 1.0 simplifies the topography near South Africa without considering the above topographic features. This is likely the reason why our experiment cannot achieve a highly consistent realization of the Agulhas retroflection characteristics and the eddy-shedding process of the Agulhas Rings. Compared to the Neverworld experiment in Khani et al. (2019), the idealized African topography in our work has a wider zonal span and smoother curvature. This might foster interactions between eddies and jets near the topographic feature, leading to less distinct individual eddy-shedding events. In addition, the idealized ridge causes energetic jets and eddy-active regions downstream. The position of the idealized African continent relative to the jets

https://doi.org/10.5194/gmd-2024-72
Preprint. Discussion started: 29 April 2024

Geoscientific Model Development
Discussions

downstream of the mid-ocean ridge also deviates from that of the realistic Southern Ocean. The flushing effect of the eddying jet is not conducive to keeping the idealized Agulhas region highly consistent with the flow characteristics of the realistic situation. This design is a compromise: if we place the African landmass further north within the existing domain at its current size, the processes in the Agulhas region would inevitably be strongly affected by the sponge layer. We prefer the simulation result in the relevant area to reflect the intrinsic eddying variability and the general effect of topography on the flow, thereby making the dataset generic for analyzing mesoscale dynamics and examining parameterization schemes. For potential future works, we suggest increasing the meridional span of the domain to allow the topographic features to be placed at a more suitable position and adopting a gentler ridge setting.

2.3 Implementation of MODNS

The fundamental requirement for MODNS is that the horizontal resolution can explicitly resolve the first baroclinic deformation radius. Under the model configuration, it is basically greater than 15 km. If we follow the experience that the model discretization can adequately represent processes exceeding five times the grid spacing, then the horizontal resolution required for MODNS should reach at least 3 km. Additionally, Marques et al. (2022) found that when the horizontal resolution reaches 1/32° in Neverworld-2, the mesoscale model performance converges, meaning that the resolution is sufficient to fully resolve mesoscale in their model. Based on these considerations, we conduct a simulation with an even finer horizontal resolution of 2 km to achieve a certain type of MODNS.

Directly running the 2 km simulation (e.g., spin up from rest) is costly. Therefore, our spin-up strategy is as follows: (1) Integrate an 8 km simulation from rest for 45 model years to reach the quasi statistical-steady state. (2) Interpolate the final output of the 8 km simulation as the initial field for the 4 km simulation and integrate for 15 model years to reach the corresponding quasi statistical-steady state. (3) Interpolate the final output of the 4 km simulation as the initial value field for the 2 km simulation and integrate for several model years. Fig. 3 shows the time series of ACC transport, domain-averaged potential temperature, and domain-averaged kinetic energy for the last few years of the 2 km simulation. There are no significant changes in the ACC transport or kinetic energy levels, and the trend of the domain-averaged potential temperature is less than 0.003°C/yr. Therefore, we conclude that the 2 km simulation reaches its corresponding quasi statistical-steady state by the sixth model year.

We employ the 7th-order monotonicity-preserving advection scheme (the MITgcm advection scheme code is 7) when running the 8 km simulation. To accelerate the computation, we choose the 3rd-order direct space-time (DST) flux limiter scheme (the MITgcm advection scheme code is 33) for the 4 km and 2 km simulations. Since the 2 km simulation has already been submesoscale-permitting, we retain the 3-day average output from the 9th model year and daily instantaneous fields from the first two months in the 10th model year in the 2km simulation to demonstrate the model performance for eddying processes of different scales, including mesoscale and submesoscale.

https://doi.org/10.5194/gmd-2024-72
Preprint. Discussion started: 29 April 2024

Geoscientific Model Development
Discussions

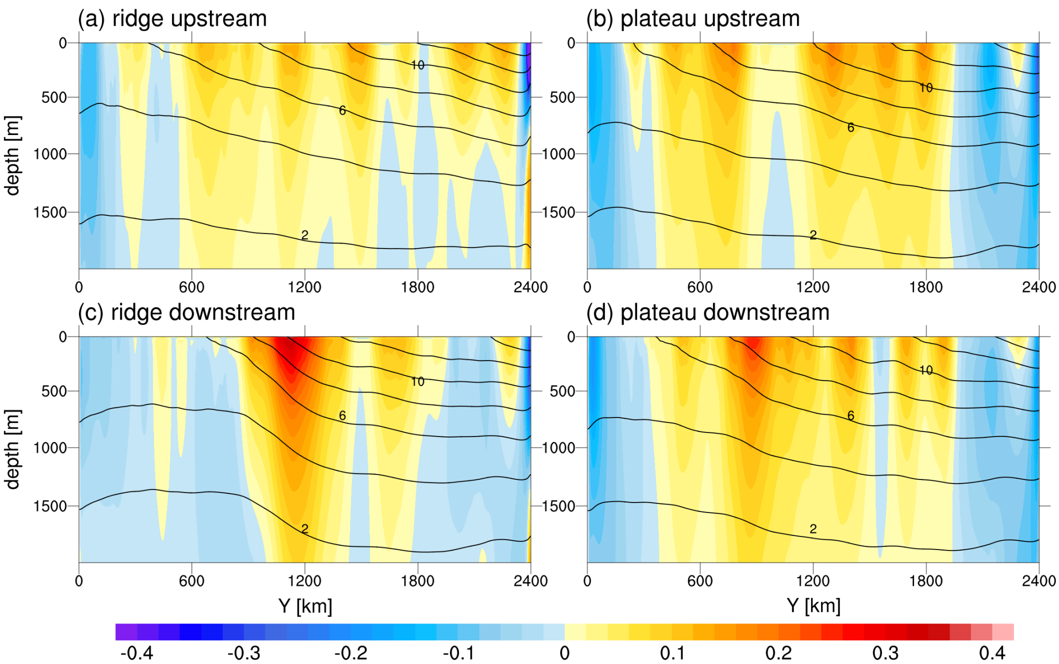

Figure 4. The Y-X profiles of the average temperature (contours) and u velocity (shading) during the 6th to 8th model year of the 2km idealized simulation. (a) X=4000km upstream of the ridge, (b) X=9500km upstream of Gaussian plateau, (c) X=6500km downstream of the ridge, and (d) X=11500km downstream of Gaussian plateau.

3 Results

In this section, we present the stratification, jets, kinetic energy spectrum, and evolution of the eddy field from the 2 km idealized Southern Ocean simulation to examine the model performance for processes relevant to oceanic mesoscale dynamics.

3.1 Stratification and jets

We show the time-averaged temperature and zonal velocity component on the Y-Z cross-sections upstream and downstream of the mid-ocean ridge and Gaussian plateau (Fig. 4). Clearly shown are the impact of large-scale topography on the overall stratification and zonal flow state. Upstream of the two bathymetric features, the zonal flow exhibits a multibranched state, accompanied by relatively gentle isotherm slopes. Downstream of large-scale topographies, the structure of the zonal flow becomes more compact, forming distinct jet cores that correspond to steeper isotherm slopes under the geostrophic constraint. In addition, the positions of the zonal flow centers drift after passing through large-scale topographic features. The above phenomena are qualitatively consistent with previous studies that used two-layer quasigeostrophic models with bottom slopes (Thompson, 2010; Chen et al., 2015; Khatri and Berloff, 2018), idealized mid-ocean ridge experiments (Abernathey and Cessi, 2014; Youngs et al., 2017), idealized Gaussian plateau experiments (Bischoff and Thompson, 2014), realistic Southern Ocean

https://doi.org/10.5194/gmd-2024-72
Preprint. Discussion started: 29 April 2024

Geoscientific Model Development
Discussions

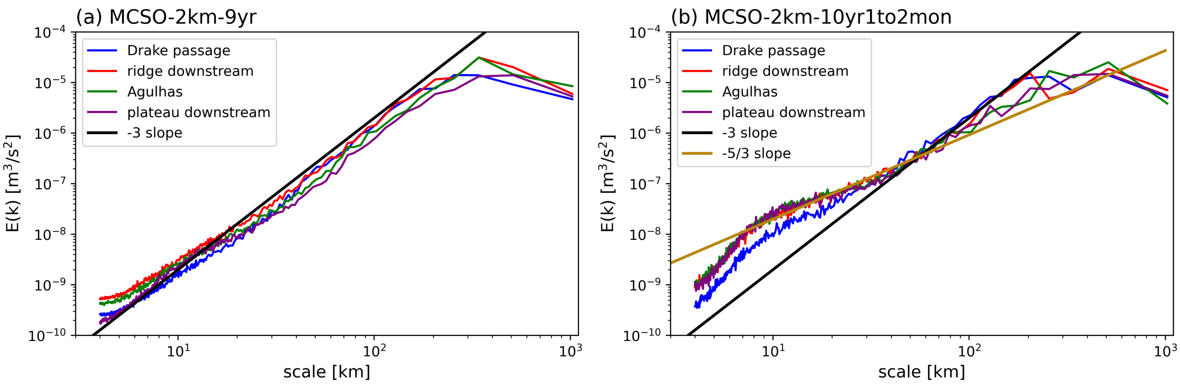

Figure 5. The averaged spectral density function of surface EKE of the 2km idealized simulation. (a) is from the 3-day-averaged output in the 9th model year, and (b) is from the snapshots in the first two months of the 10th model year. Lines with different colors represent different sampling positions. The eddy velocity is defined as subtracting the time and zonal average of a 1024km zonal segment of meridional velocity in each position.

topography simulations (Thompson and Naveira-Garabato, 2014), Southern Ocean reanalysis data (Lu and Speer, 2010; Abernathey and Cessi, 2014), laboratory experiments (Rhines, 2006), and observational data (Orsi et al., 1995; Thompson and Sallee, 2012; Chapman et al., 2020). This indicates that ISOM 1.0 is capable of describing the large-scale background processes that are closely associated with mesoscale phenomena in the Southern Ocean.

3.2 EKE spectrum

To better extract eddy signals, we take 1024 km zonal segments at given locations and compute the EKE spectrum from the meridional component of eddy velocity, similar to Marques et al. (2022). We define the eddy velocity by subtracting the annual mean and zonal segment-mean velocity. Fig. 5a shows the EKE spectrum of the 2 km simulation in the 9th model year. The raw model output in the year is of 3-day average. Thus, high-frequency processes (e.g., submesoscale) are filtered out, and the output highlights the model performance in simulating mesoscale processes. In regions with active mesoscale eddies, including the Drake Passage, downstream of the mid-ocean ridge, the Agulhas region, and downstream of the Gaussian plateau, the results consistently exhibit a -3 spectral slope. This result suggests that the model excellently describes oceanic mesoscale motions that can be regarded as quasigeostrophic turbulence and theoretically possesses a k^{-3} (k is wavenumber) kinetic energy spectrum (Charney, 1971; Fu and Morrow, 2013; Vallis, 2017).

Fig. 5b shows the EKE spectrum computed from the daily instantaneous fields of the first 60 model days in the 10th year of the 2 km simulation. We find that at scales greater than 30 km, the spectral slopes in representative areas are essentially close to -3, demonstrating the characteristics of mesoscale dynamics. Within the scale range of 8-30 km, the 2 km simulation exhibits a spectral slope closer to -5/3 in the Agulhas region, downstream of the Gaussian plateau, and the mid-ocean ridge, showing characteristics of submesoscale processes that comply with surface quasigeostrophic dynamics (Blumen, 1978; Held et al.,

https://doi.org/10.5194/gmd-2024-72
Preprint. Discussion started: 29 April 2024

1995; Lapeyre, 2017). However, the spectral slope in the idealized Drake Passage is steeper than -5/3, showing characteristics of submesoscale processes that conform to surface quasigeostrophy with ageostrophic advection, which theoretically have a kinetic energy spectral slope of -2 (Boyd, 1992; Callies and Ferrari, 2013). The spectral slope steepens on scales smaller than 8 km, and the effect of dissipative schemes emerges.

From the above, we can explain why the 2 km simulation yields such an energetic mesoscale eddying field. (1) The horizontal resolution is high enough to resolve the deformation radius and some submesoscale processes. Schubert et al. (2020) showed that mesoscale eddies can grow by absorbing submesoscale eddies generated by mixed-layer baroclinic instability. We find (see the next section) that although mesoscale eddies do not always successfully absorb submesoscale processes, submesoscale phenomena are boosters of the specific developmental and evolutionary trajectories of mesoscale processes. Considering the contribution of submesoscale processes to multiscale oceanic dynamics (Taylor and Thompson, 2023), identifying submesoscale signals is beneficial for enhancing mesoscale model performance. (2) The affected scales of the applied dissipative schemes are sufficiently smaller than the first baroclinic deformation radius. Therefore, these schemes do not directly contaminate the simulated mesoscale dynamics. In summary, the 2 km idealized Southern Ocean simulation output can be considered a type of MODNS dataset.

3.3 Examples of multiscale eddy interactions

In this section, we directly examine the performance of the 2 km idealized model in simulating the evolution of eddying processes. Fig. 6 shows snapshots of the sea surface temperature (SST), sea surface height anomaly (SSHA), sea surface kinetic energy, and Rossby number (Ro) in the Agulhas region. The Rossby number is defined as the ratio of the vertical component of relative vorticity $\zeta = v_x - u_y$ to the local Coriolis parameter $f = f_0 + \beta y$. The Rossby number can indicate the relative activity level of submesoscale and mesoscale processes in the flow (Thomas et al., 2008; Schubert et al., 2019). When mesoscale processes dominates the flow, $|Ro| \ll O(1)$. When submesoscale processes are active, $|Ro| \sim O(1)$.

Fig. 6 contains large amount of information. The region is experiencing highly complex processes, including mesoscale eddies, jets, submesoscale processes, and their multiscale interactions. To maintain a coherent narration, we divided the events occurring in this area into three episodes: (1) interactions between large mesoscale eddies in the central region, (2) interactions among mesoscale eddies, meandering jets, and submesoscale processes on the right, and (3) multiple eddy interactions on the left.

3.3.1 Episode I

First, we discuss the simplest event occurring in the central area, where two eddies of similar size form a mesoscale dipole and interact closely with each other. Since both cold and warm eddies exhibit complete and independent cores in the SSHA field (Fig. 6a and b), they can be regarded as typical geostrophic eddies. In the region between eddy cores, the circulation directions of the two eddies are consistent, leading to a noticeable increase in the flow (Fig. 6c). With respect to the Rossby number (Fig. 6d), these large eddies with spatial scales exceeding 100 km do not have intense submesoscale signals in their main body. The cold eddy shows slightly stronger submesoscale signals in its core than the warm eddy does. Strong submesoscale signals

https://doi.org/10.5194/gmd-2024-72
Preprint. Discussion started: 29 April 2024

Geoscientific Model Development Discussions

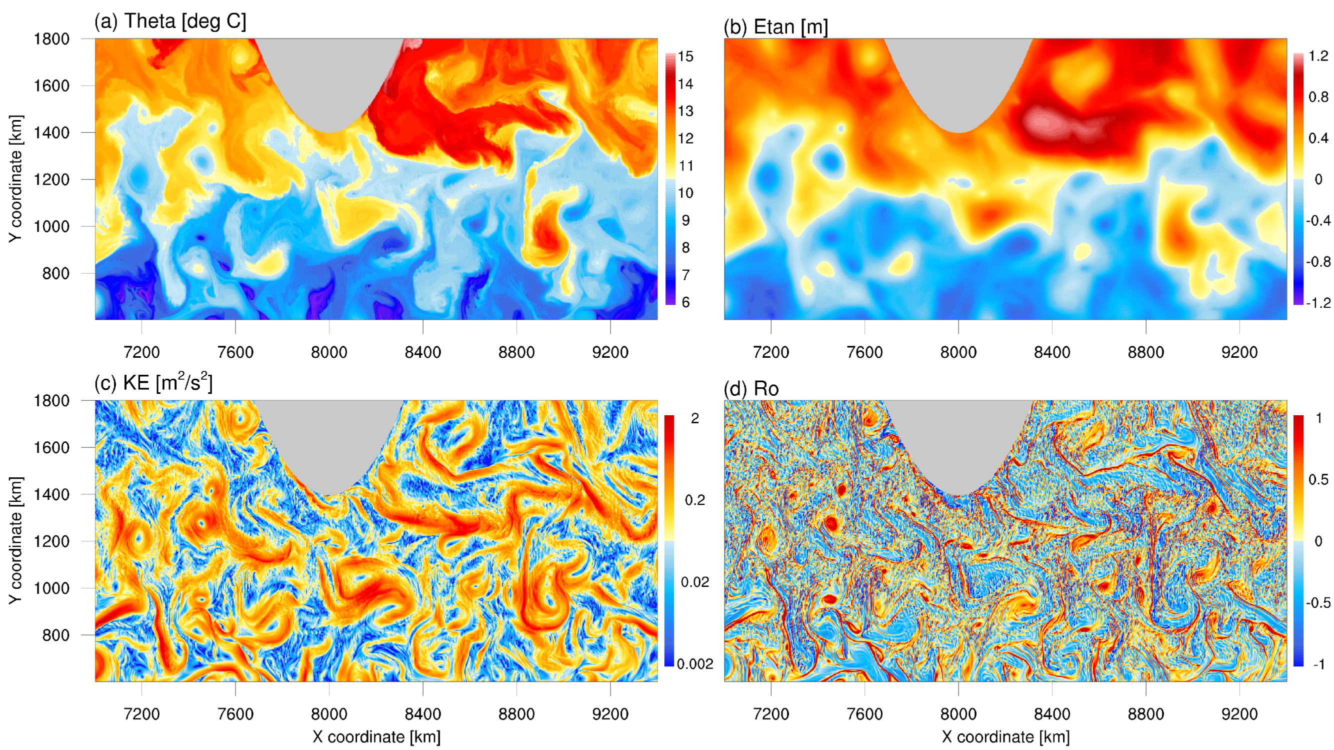

Figure 6. Surface snapshot of the 27th model day in the 10th model year of the 2km simulation in Agulhas area. (a) Potential temperature, (b) the linearized free surface height or sea surface height anomaly, (c) kinetic energy, and (d) Rossby number (defined as relative vorticity divided by local Coriolis parameter).

appear in filaments along the temperature fronts surrounding the mesoscale eddy, with alternating signs. These results are qualitatively consistent with the submesoscale phenomena obtained by Schubert et al. (2020) using the Agulhas region model with a horizontal resolution of $1/60°$ and by Gula et al. (2014) and McWilliams (2016) using the Gulf Stream regional model with a hundred-meter horizontal resolution.

3.3.2 Episode II

We now focus on the fascinating story of interactions among mesoscale eddies, meandering jets, and submesoscale processes in the right half of the region (Fig. 6). In the SST field (Fig. 6a), the main features include the intense southward intrusion of warm water along the eastern coast of the continent (Event A), a large mesoscale warm eddy connected to the warm water mass through a filamentary structure (Event B), and another southward intrusion of warm water on the far right (Event C). All of them can show closed structures in the SSHA field (Fig. 6b), implying that they possess energetic geostrophic flows. In the kinetic energy field (Fig. 6c), southward warm water intrusions (Events A and C) are connected by a powerful, meandering jet. The jet spans over 1000 km along the flow direction and less than 200 km in the perpendicular direction.

https://doi.org/10.5194/gmd-2024-72
Preprint. Discussion started: 29 April 2024

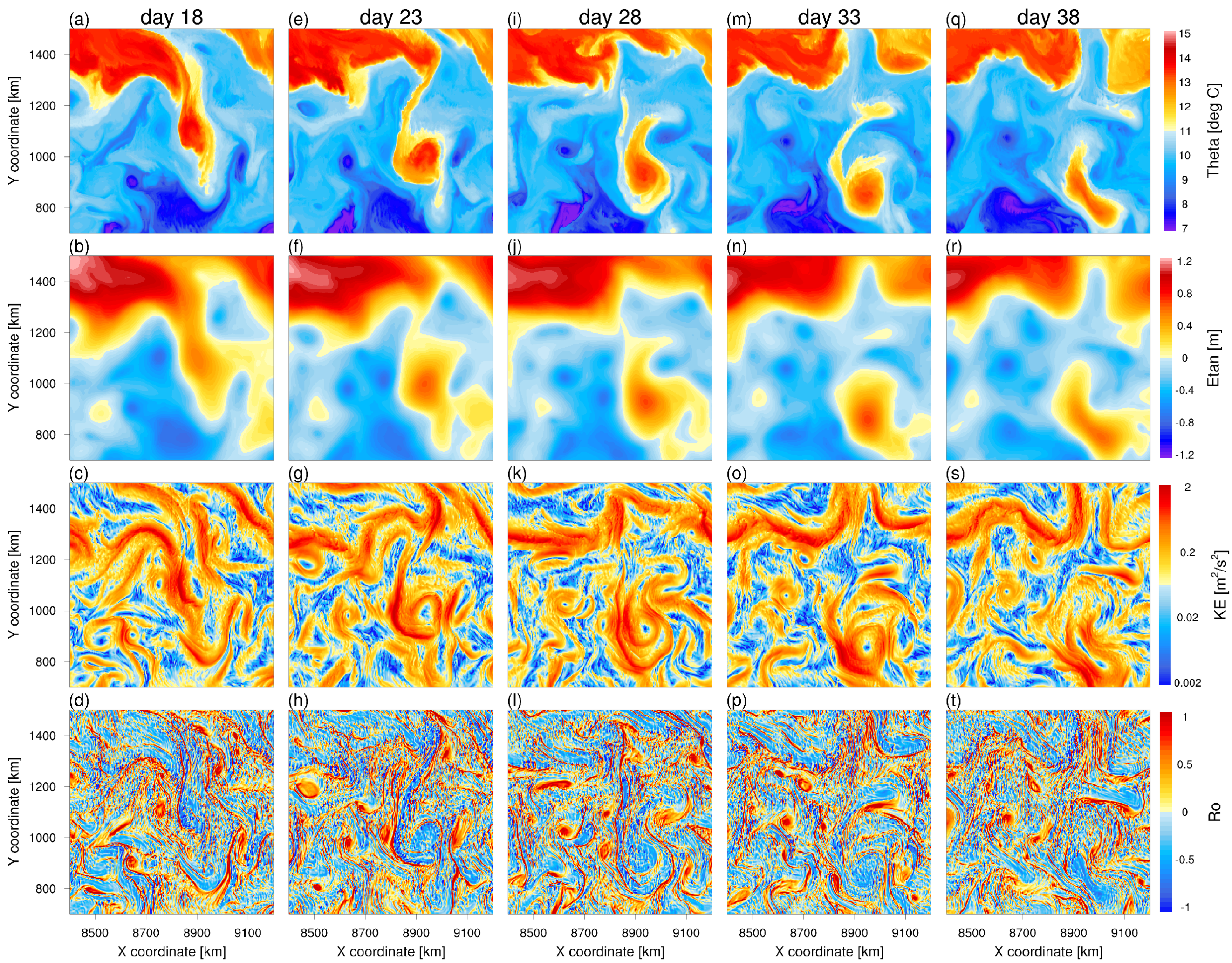

Figure 7. An example for warm eddy and meandering jet evolution. From top to bottom are the potential temperature, the linearized free surface height, kinetic energy, and Rossby number.

It aligns with the temperature front and the southern edge of the positive SSHA regions, which shows geostrophy. The warm eddy in the southern region (Event B) exhibits a cyclonic inward-curving motion. The filament connecting the eddy to the warm water in the north shows energy levels significantly higher than those of the background environment and possesses distinct submesoscale characteristics (Fig. 6d). The warm eddy collides with a cold eddy to the northeast and simultaneously affects several small cold eddies to the west. We can find traces of multiscale interactions from Ro (Fig. 6d). Strong submesoscale signals occur near the temperature front and along the filament. In addition, cold eddies tend to have smaller spatial scales and compact structures, with cores dominated by submesoscale features. Warm eddies often have larger spatial scales and looser internal structures, with submesoscale features mainly appearing at the edges of spiral structures.

To vividly illustrate the multiscale interactions in the right half of Fig. 6, Fig. 7 shows the shedding process of the warm eddy and the evolution of the meandering jet.

On day 18, southward warm water intrusion occurs east of the continent (Fig. 7a). The southernmost part of the water mass begins to rotate counterclockwise and presents a closed individual SSHA center (Fig. 7b) as well as a nearly closed circular flow in the kinetic energy field (Fig. 7c). In the Ro field (Fig. 7d), small cold eddies on the east and west sides of the warm water mass shear the connecting part, thereby assisting the warm eddy shedding from the water mass. Several intermittent mesoscale jets follow the temperature front (northwest-southeast direction).

On day 23, the main body of the warm eddy detaches from the water mass, and only a slender filament connects them in the SST field (Fig. 7e). The filamentary structure has a spatial scale of approximately 20 km perpendicular to its flow direction, and it is not entirely a geostrophic process (i.e., the SSHA field in Fig. 7f cannot visually express it). The kinetic energy and Ro field (Fig. 7g and h) verify that the filament has intense ageostrophic submesoscale signals. In addition, the warm eddy has an almost organized internal structure and exhibits a closed circulation. The jet that was oriented northwest-southeast on day 18 has broken and forked, with its southern part absorbed by the warm eddy and its northern part moving toward the frontal jet along the edge of another warm water mass.

On day 28, the filament breaks, and the warm eddy sheds from the warm water mass (Fig. 7i). The warm eddy organizes around a circular center in the SSHA field (Fig. 7j). The absorbed southern jet becomes the outer circulation of the warm eddy (Fig. 7k). The remaining northern jet merges with another frontal jet along the eastern warm water mass, temporarily forming a zonal jet that spans over 1000 km. Over the past ten days, cold eddies near the warm eddy have also developed synchronously. Their numbers have increased, their cores have become more compact, and their role has shifted from facilitating the detachment of the warm eddy (Fig. 7d and h) to directly confronting the warm eddy (Fig. 7l).

On day 33, the warm eddy with a long tail moves further away from the warm water mass (Fig. 7m), and its main body has an independent SSHA center and multi-loop circulation (Fig. 7n and o). The warm eddy engages in drastic interactions with the surrounding cold eddies (Fig. 7p) and attempts to integrate them into its circulation (Fig. 7o). The cold eddy to the northeast of the warm eddy undergoes significant strain and stimulates more fierce submesoscale signals. The cold eddy to the west of the warm eddy also experiences noticeable stretching. However, the confrontation among eddies has no winner this time. On day 38 (Fig. 7q-t), the structure of cold eddies adjacent to the warm eddy is essentially torn apart, and the structure of the warm eddy itself is also compromised. The warm eddy is drawn toward the southern domain with cold background temperature, inevitably entering the recession stage. Meanwhile, the meandering jet in the north breaks due to excessive meridional fluctuations.

3.3.3 Episode III

We now examine the eddy-eddy interactions in the left half of Fig. 6. Most eddies in this region are cold eddies and vary in size. If characterized by a circular structure in the kinetic energy field (Fig. 6c), small cold eddies have a spatial scale of about 50 km, while large cold eddies have a spatial scale of approximately 200 km. These cold eddies generally have compact cores accompanied by significant submesoscale signals (Fig. 6d).

https://doi.org/10.5194/gmd-2024-72
Preprint. Discussion started: 29 April 2024

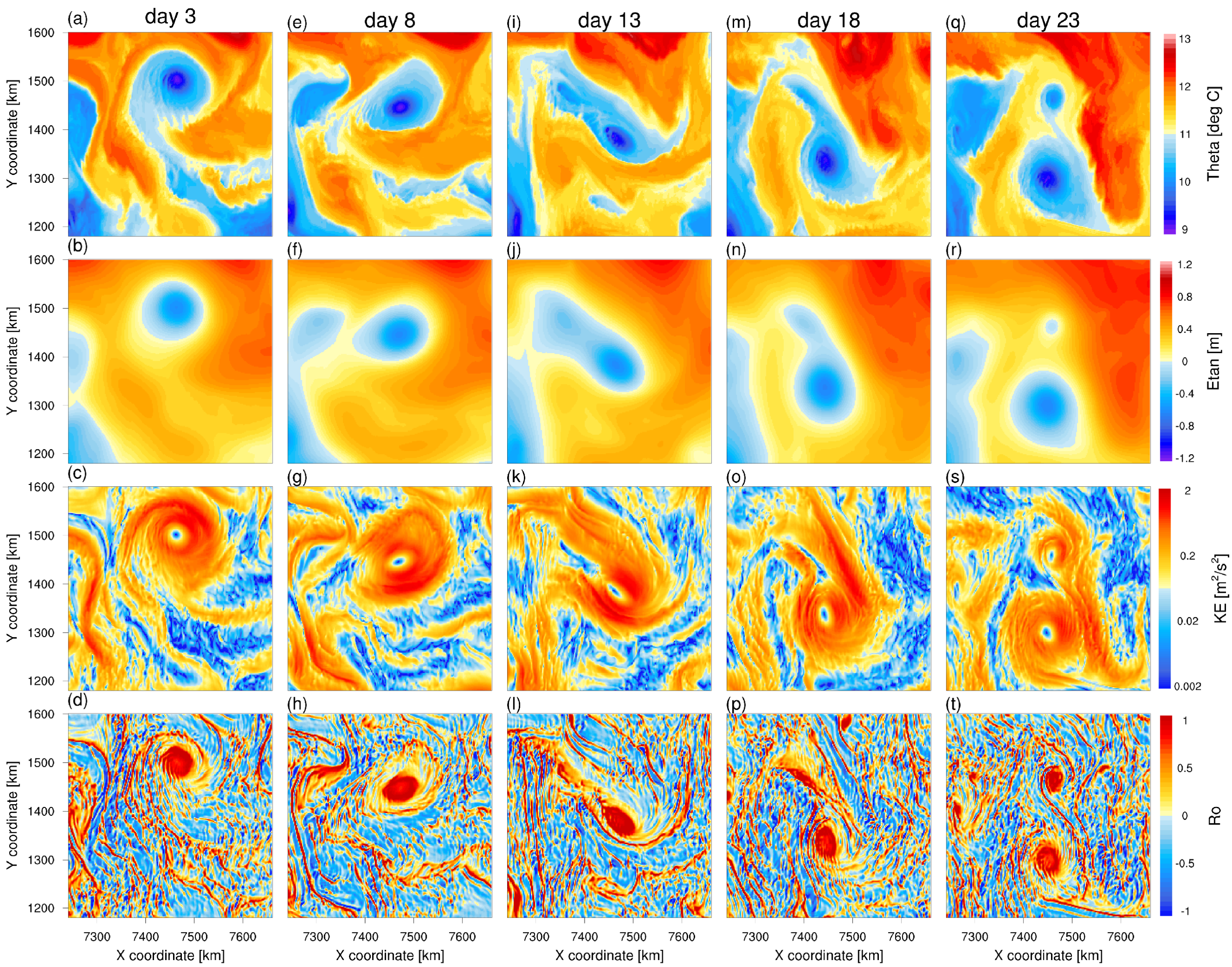

Figure 8. An example for cold eddy evolution.

To vividly illustrate the features of cold eddies and their interactions, we select an eddy centered roughly at (x, y) = (7450 km, 1300 km) on day 27 (i.e., Fig. 6) as an example and examine its evolution (Fig. 8).

On day 3, the eddy (eddy A) is a fully developed mesoscale cold eddy with a compact core (Fig. 8a-d). To the west of the eddy, a warm water intrusion event occurs, and another cold water mass exists. Submesoscale signals mainly appear in the cold eddy core, areas of rapidly rotating peripheral circulation, and areas with strong temperature gradients.

On day 8, the cold eddy moves southeastward. Another cold eddy (eddy B) embryo develops in the cold water mass on the west side of eddy A (Fig. 8f). Eddy A and B have opposite flows in the intermediate area, thus strongly shearing the warm

https://doi.org/10.5194/gmd-2024-72
Preprint. Discussion started: 29 April 2024

water between them (Fig. 8e). Affected by the cold eddy embryo, the shape of eddy A undergoes slight deformation, but its structure is still compact (Fig. 8g and h).

On day 13 and day 18, eddy A continues to move southeastward and tries to absorb eddy embryo B (Fig. 8i-p). The Rossby number (Fig. 8l and p) shows that the absorption process excites intense submesoscale signals in the field. Eddy A is the dominant player in the interaction, and one might easily assume that eddy A would smoothly engulf small eddy embryo B.

Nevertheless, eddy embryo B surprisingly reinforces its core through submesoscale signals excited in the peripheral field. On day 23 (Fig. 8q-t), eddy A finally fails to absorb eddy embryo B. Eddy A ultimately helps eddy B organize a compact structure. The newly formed cold eddy shows a weak closed center in the SSHA field but exhibits a complete structure in the SST and kinetic energy fields. A large Rossby number covers almost the entire eddy B. Therefore, it is essentially a strong submesoscale eddy.

The above examples demonstrate the diversity and high complexity of multiscale interactions related to mesoscale processes. Under conditions with energetic mesoscale activities and high eddy number density, submesoscale phenomena are boosters of the specific developmental and evolutionary trajectories of mesoscale processes. Therefore, an appropriate representation of submesoscale processes in OGCMs is crucial for improving the simulations of mesoscale dynamics. The most straightforward approach is to improve the horizontal resolution. ISOM 1.0 with the horizontal resolution of 2 km not only explicitly resolves the first baroclinic deformation radius but also captures a significant portion of submesoscale processes. This helps to obtain a highly consistent k^{-3} EKE spectrum as shown in Fig. 5, and ensures that the simulation results are sufficient to be considered a form of MODNS dataset. On the other hand, when constrained by computational and storage resources, if one wants to achieve such simulation improvements, one might have to introduce energetically optimized schemes (Jansen and Held, 2014; Jansen et al., 2019; Bachman, 2019) or parameterizations targeting specific submesoscale processes (Fox-Kemper and Ferrari, 2008; Bachman et al., 2017b; Yankovsky et al., 2021; Zhang et al., 2023) or LES techniques (Fox-Kemper and Menemenlis, 2008; Bachman et al., 2017a; Khani and Dawson, 2023) rather than adopting only dissipative schemes to maintain computational stability.

4 Multipassive tracer tests

We use ISOM 1.0 to conduct multipassive tracer tests in this section. Multiple passive tracers can be leveraged as samples to construct an overdetermined linear system of equations to estimate the eddy transport tensor(Bachman et al., 2015, 2020). A two-dimensional diagnosis (i.e., on the neutral surface) requires at least two nonparallel samples, and a three-dimensional diagnosis (i.e., on the z-coordinate) needs at least three nonparallel samples(Xie et al., 2023). We conduct online tests of passive tracers using the 8 km simulation of the 46th to 49th model years (the flow is the same for all tracers). We uncover the properties of passive tracers in ISOM 1.0 and propose guidelines for selecting passive tracer combinations, thereby providing technical references for works that employ relevant methods for eddy transport diagnosis and parameterization design.

Geoscientific Model Development
Open Access
Discussions

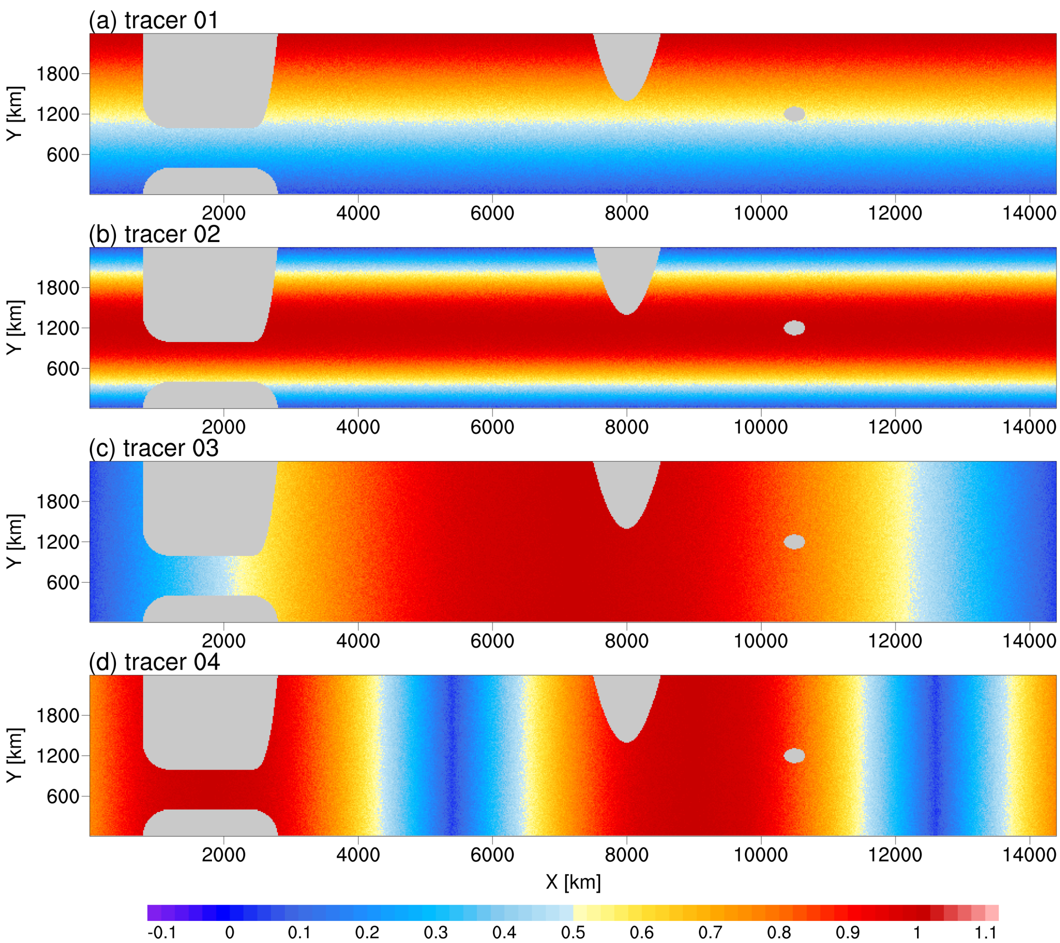

Figure 9. The initial fields for the recommended passive tracers.

All passive tracers in the manuscript obey the advection equation without diffusion and source/sink terms (i.e., no restoration to a prescribed profile). That is,

$$\frac{\partial C_i}{\partial t} + \mathbf{u} \cdot \nabla C_i = 0 \tag{10}$$

The only difference among tracers lies in their initial fields. To ensure that the tracers are mutually independent (i.e., have very low spatial correlation), we recommend the initialization of a combination of four passive tracers as follows: (Fig. 9):

$$C_1(x,y,z,t_0) = y/L_y + \sigma_1(x,y,z) \tag{11}$$

$$C_2(x,y,z,t_0) = sin(\pi y/L_y) + \sigma_2(x,y,z) \tag{12}$$

https://doi.org/10.5194/gmd-2024-72
Preprint. Discussion started: 29 April 2024

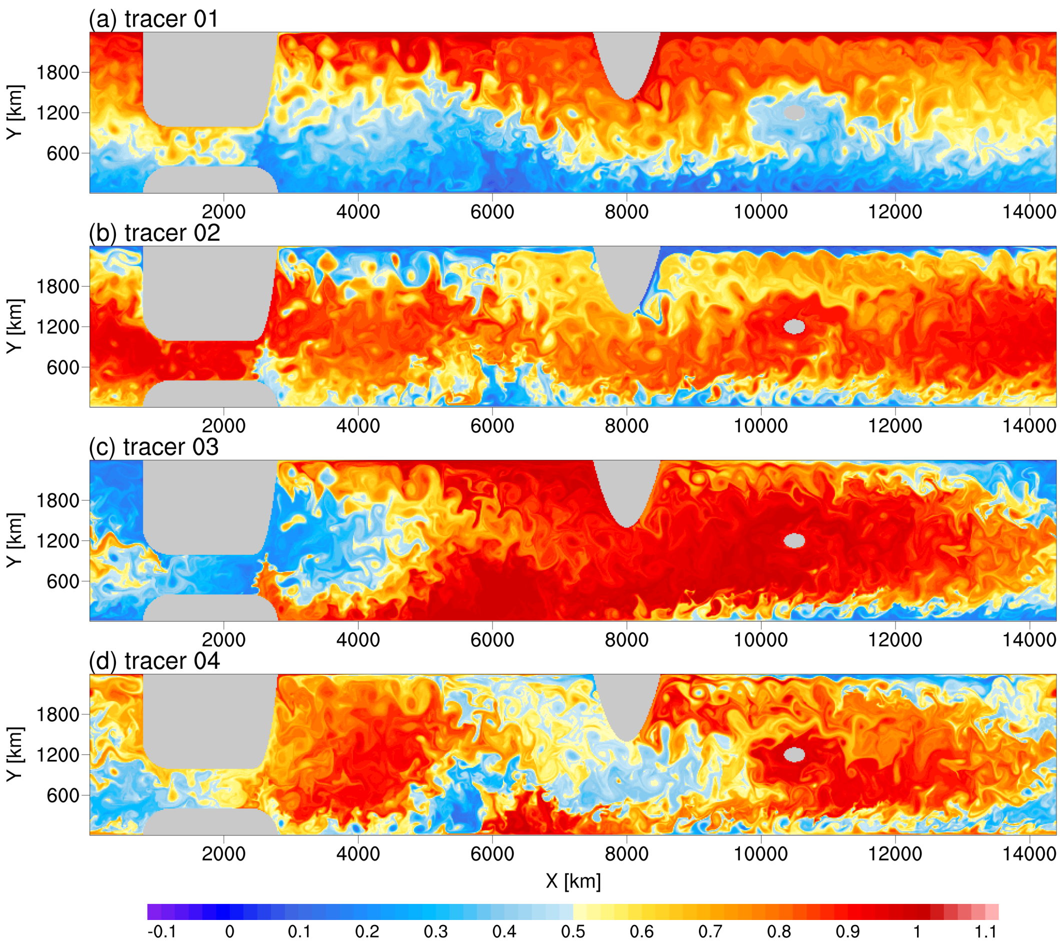

Figure 10. Snapshot of day 360 in the multi-passive-tracer experiment.

$$C_3(x,y,z,t_0) = sin(\pi x/L_x) + \sigma_3(x,y,z) \tag{13}$$

$$C_4(x,y,z,t_0) = |sin(2\pi x/L_x + \pi/4)| + \sigma_4(x,y,z) \tag{14}$$

The random terms σ_i $(i = 1,2,3,4)$ follow a uniform distribution between 0 and 0.1. We further limit the initial fields within the range of 0 to 1. The setup ensures that the absolute Pearson correlation coefficients between tracers are far less than 0.1, and the initial fields can be considered mutually independent. Their spatial standard deviations are at the same level (approximately 0.3). This allows each tracer to contribute almost equally when solving the overdetermined linear system related to the transport tensor.

https://doi.org/10.5194/gmd-2024-72
Preprint. Discussion started: 29 April 2024

Geoscientific Model Development
Discussions

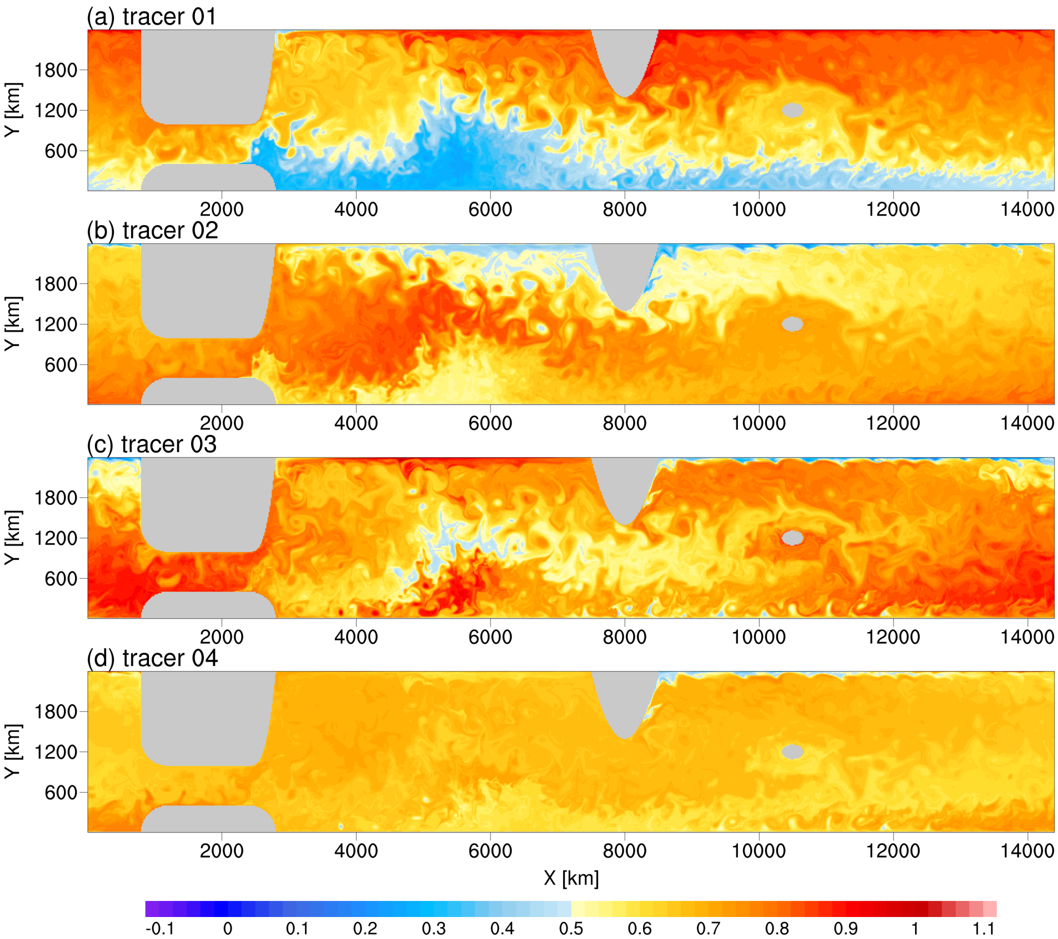

Figure 11. Snapshot of day 1410 in the multi-passive-tracer experiment.

After long-term stirring by the flow, the homogenization of individual passive tracers occurs, and the spatial pattern among tracers becomes correlated (Fig. 10 and 11). This leads to the disappearance of the tracer gradient and the local alignment of the eddy flux vectors among tracers. Both effects can cause the failure of the multipassive tracer method for diagnosing transport tensors based on the flux-gradient relationship. There are two approaches to address these issues. The first approach is to add a restoration term to relax tracers to prescribed profiles. When diagnosing the transport tensor, one must address the problems caused by the restoration term (Bachman et al., 2015, 2020; Haigh and Berloff, 2021). The second approach is to continue to adopt passive stirring but release tracers several times(Wei and Wang, 2021). We prefer the latter approach and conduct validation tests. The key is to explore the time scale of homogenization and the correlation of the passive tracer combination. As long as the time interval of the release is shorter than the time scale at which unacceptable homogenization and correlation occur, the tracer output is suitable for subsequent diagnosis.

https://doi.org/10.5194/gmd-2024-72
Preprint. Discussion started: 29 April 2024

Geoscientific Model Development
Discussions

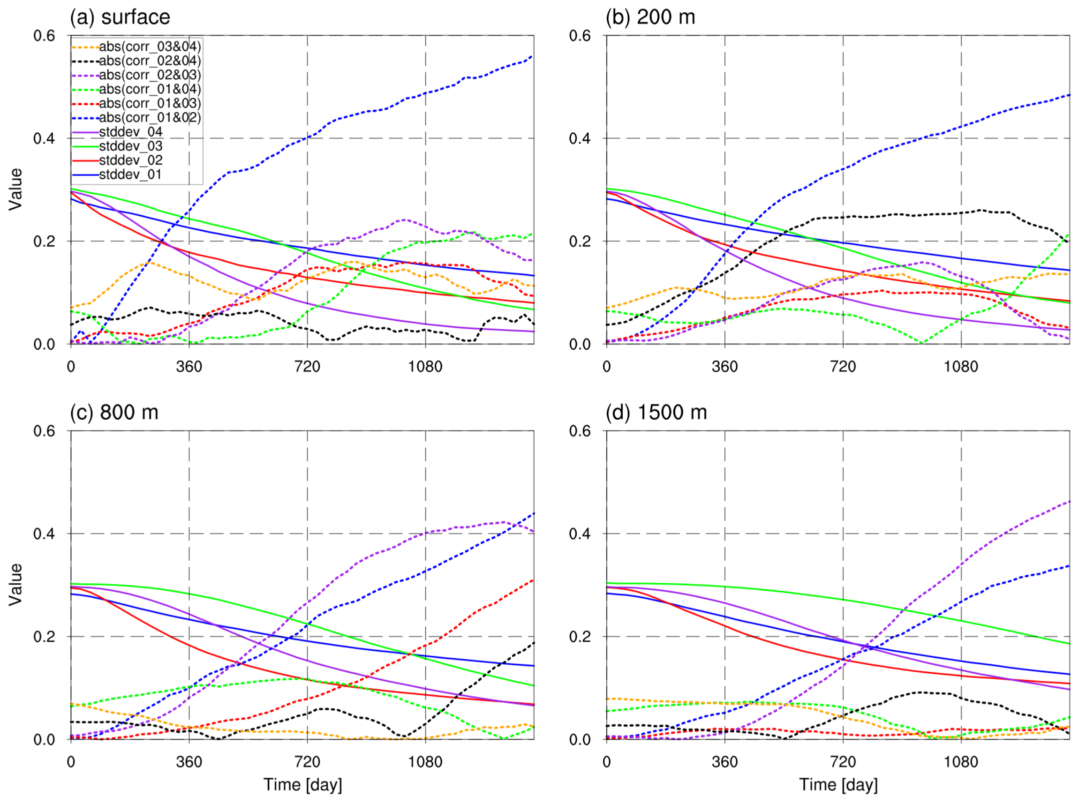

Figure 12. The temporal evolution of the standard deviation of tracers (solid line) and the absolute spatial correlation between tracers (dashed line) at different depths.

We test various initial tracer fields to explore how to delay the homogenization process and ensure the mutual independence of the tracers. We share noteworthy guidelines as follows.

(1) If the flow is quasi two-dimensional (e.g., large-scale oceanic motion), the initial tracer field should vary horizontally. One should avoid setting more than one initial field that changes only in the z-direction, such as $C(z) = |z|/H$ and $C(z) = sin(\pi|z|/H)$. Although these two expressions appear to be independent, they are highly correlated in the horizontal plane.

(2) If the domain has periodic boundaries, discontinuities in the initial fields at the corresponding boundaries should be avoided. We test a passive tracer with an initial field of $C(x) = x/L_x$. Though it seems not to cause significant numerical issues under the 7th-order monotonicity-preserving advection scheme, there is no guarantee that such an initial field setting would not be problematic when using lower-order schemes or spectral methods.

(3) A crucial principle is that the initial tracer fields should be dominated by structures with large spatial scales. Otherwise, the tracer fields would be rapidly mixed by flow stirring. An extreme example is complete random initialization, which fills the tracer field with small-scale noise and can be homogenized within days. Another example is the initial field with two meridional half-period harmonic waves, $C(y) = |sin(2\pi y/L_y)|$. Though its spatial scale is far larger than that of random

https://doi.org/10.5194/gmd-2024-72
Preprint. Discussion started: 29 April 2024

noise, it can be significantly mixed over a few months. Among the four tracers recommended in the paper, tracer C_4, which has an initial field with two zonal half-period harmonic waves, homogenizes the fastest in the upper layer and reduces its spatial standard deviation by over 40% in the first year (the purple solid line in Fig. 12). Tracer C_2, with an initial field of a meridional half-period wave, homogenizes the fastest in the mid-layer and reduces its spatial standard deviation by more than 50% within two years (the red solid line in Fig. 12). The homogenization rates of tracers C_1 and C_3, which have larger spatial scales, are significantly lower (the blue and green solid lines in Fig. 12).

By further analyzing the temporal evolution of the absolute Pearson correlation between the four passive tracers (dashed lines in Fig. 12), we find that: (1) the spatial correlation between tracers generally increases over time. This indicates that their spatial patterns tend to be similar under the continuous stirring of the same flow. (2) The evolution of correlations at different depths varies. Taking 720 model days as an observation point, we find that deeper locations generally have slower increase in absolute correlation. (3) Within 360 model days, at least three tracers can always maintain a low spatial correlation, and the spatial distribution of each tracer has not yet visually shown homogenization (Fig. 10). By the 720th model day, three tracers (except tracer C_2) could maintain a low correlation. Therefore, under the condition of ISOM 1.0, controlling the duration of tracer release to less than 2 model years enables homogenization and correlation to be limited to an acceptable level so that the multiple tracer combination can serve as samples for accurately estimating the transport tensor.

5 Conclusions

In this paper, we introduce an idealized Southern Ocean model that contains a simplified version of iconic topographic features in the Southern Ocean. We conduct a fully mesoscale eddy-resolving (2 km) simulation. The prominent feature of the model is the successful simulation of a fully developed and vigorous mesoscale eddying field. We reproduce the EKE spectrum of k^{-3} predicted by geostrophic turbulence theory. In addition, the simulated geographical distribution of eddy activities is qualitatively consistent with the realistic situation, and the model can describe the topographic effect on stratification and large-scale flow.

To facilitate a smoother introduction of LES methods into ocean mesoscale parameterization, we propose the concept of MODNS. Its model grid should explicitly resolve the first baroclinic deformation radius, and the scales where dissipative schemes play a significant role are distant from the mesoscale dynamical regime, making it the benchmark for a priori and a posteriori tests of LES models or MOLES schemes into OGCMs. The 2 km idealized simulation satisfies the demands for MODNS and captures a portion of the submesoscale processes. Therefore, it can serve as a type of MODNS and offer reliable data support for conducting relevant a priori and a posteriori tests.

We demonstrate the diversity and high complexity of multiscale eddy interactions related to mesoscale processes by examining the evolution of mesoscale eddies, submesoscale phenomena, and meandering jets. When the field experiences energetic mesoscale activities and a high eddy number density, submesoscale phenomena are boosters of the specific developmental and evolutionary trajectories of mesoscale processes. Therefore, expressing the collective effect of submesoscale processes in OGCMs is beneficial for simulating mesoscale variabilities.

https://doi.org/10.5194/gmd-2024-72
Preprint. Discussion started: 29 April 2024

In addition, we use the idealized model to conduct multipassive tracer experiments. We reveal some guidelines for the initialization settings of passive tracers. We discover a combination of four passive tracers that can delay the homogenization process and ensure the mutual independence of tracers for a long time. With this combination and in ISOM 1.0, controlling the duration of each experiment of tracer release to less than 2 model years can ensure that the spatial standard deviation of the tracers and the correlations among the tracers are limited to acceptable levels. This allows the results from multiple release experiments of the tracer combination to form a qualified sample for solving the eddy transport tensor based on the flux-gradient relationship.

Global oceanic motion is a complex process involving multiple spatiotemporal scales, and large-scale background dynamics vary across different regions. The idealized model in this paper provides a type of MODNS as a simplification of Southern Ocean processes. Similarly, other idealized models, such as the double-gyre basin model, can also be used to generate corresponding MODNS datasets. The LES schemes and their matching parameters applicable might differ under different basic flows. Therefore, we should evaluate LES-related methods across idealized and realistic models. In addition, the setting for diapycnal parameterization in the simulation is simple, and mixed layer processes are likely to be underexpressed. Thus, using MODNS data for designing pure submesoscale parameterization schemes is inappropriate. Improving the horizontal resolution and optimizing the simulation of submesoscale processes in the mixed layer to generate a type of submesoscale ocean DNS is also an orientation for future work.

Code and data availability. The dataset, configuration files, and codes needed for the idealized simulation are publicly available in Science Data Bank (https://doi.org/10.57760/sciencedb.iap.00012). The MITgcm software and documentation are available at http://mitgcm.org/. The Southern Ocean State Estimate is available online (http://sose.ucsd.edu/sose_stateestimation_data_05to10.html and http://sose.ucsd.edu/BSOSE6_iter106_solution.html).

Author contributions. JX was involved in conceptualization, conducting the simulation, programming, visualization, formal analysis, and writing the original draft. XW was involved in conceptualization, conducting the simulation, programming, and visualization. HL was involved in the conceptualization, formal analysis, supervision, and revision of the manuscript. PL was involved in conceptualization and formal analysis. JY was involved in conceptualization, formal analysis, and data processing. ZY was involved in the conceptualization of the paper and implementation of the software on EarthLab. All authors contributed to writing and revising the paper.

Competing interests. The authors declare that they have no known competing financial interests or personal relationships that could have appeared to influence the work reported in this paper.

https://doi.org/10.5194/gmd-2024-72
Preprint. Discussion started: 29 April 2024

Geoscientific Model Development
Discussions

Acknowledgements. We express our gratitude to all the contributors to MITgcm and SOSE. We appreciate the patience and effort of the editor and reviewers. We thank Hao Fu for the enlightening discussion. We thank the support from the "Earth System Science Numerical Simulator Facility" (EarthLab). This study was financially supported by the National Natural Science Foundation of China (92358302), the National Key R&D Program for Developing Basic Sciences (2022YFC3104802), and the Tai Shan Scholar Program (Grant No. tstp20231237).

Financial support. This study was supported by the National Natural Science Foundation of China (92358302), the National Key R&D Program for Developing Basic Sciences (2022YFC3104802), and the Tai Shan Scholar Program (Grant No. tstp20231237).

Geoscientific Model Development Discussions
Open Access

References

Abernathey, R. and Cessi, P.: Topographic Enhancement of Eddy Efficiency in Baroclinic Equilibration, Journal of Physical Oceanography, 44, 2107–2126, https://doi.org/10.1175/JPO-D-14-0014.1, 2014.

Abernathey, R., Marshall, J., and Ferreira, D.: The dependence of Southern Ocean meridional overturning on wind stress, Journal of Physical Oceanography, 12, https://doi.org/10.1175/JPO-D-11-023.1, 2011.

Adcroft, A., Campin, J.-M., Doddridge, E., and Dutkiewicz, S.: MITgcm Documentation, Release checkpoint68u-7-gfbfa6b7, https://doi.org/https://doi.org/10.5281/zenodo.1409237, 2024.

Alfonsi, G.: On Direct Numerical Simulation of Turbulent Flows, Applied Mechanics Reviews, 64, 020 802, https://doi.org/10.1115/1.4005282, 2011.

Artana, C., Ferrari, R., Bricaud, C., Lellouche, J. M., Garric, G., Sennéchael, N., Lee, J. H., Park, Y. H., and Provost, C.: Twenty-five years of Mercator ocean reanalysis GLORYS12 at Drake Passage: Velocity assessment and total volume transport, Advances in Space Research: The Official Journal of the Committee on Space Research(COSPAR), https://doi.org/10.1016/j.asr.2019.11.033, 2021a.

Artana, C., Provost, C., Poli, L., Ferrari, R., and Lellouche, J.-M.: Revisiting the Malvinas Current Upper Circulation and Water Masses Using a High-Resolution Ocean Reanalysis, Journal of Geophysical Research: Oceans, 126, e2021JC017 271, https://doi.org/10.1029/2021JC017271, 2021b.

Bachman: The GM plus E closure: A framework for coupling backscatter with the Gent and McWilliams parameterization, Ocean Modelling, 136, 85–106, https://doi.org/10.1016/j.ocemod.2019.02.006, 2019.

Bachman, Fox-Kemper, B., and Bryan, F.: A tracer-based inversion method for diagnosing eddy-induced diffusivity and advection, Ocean Modelling, 86, 1–14, https://doi.org/10.1016/j.ocemod.2014.11.006, 2015.

Bachman, Fox-Kemper, B., and Pearson, B.: A scale-aware subgrid model for quasi-geostrophic turbulence, Journal of Geophysical Research: Oceans, 122, 1529–1554, https://doi.org/10.1002/2016JC012265, 2017a.

Bachman, Fox-Kemper, B., and Bryan, F.: A Diagnosis of Anisotropic Eddy Diffusion From a High-Resolution Global Ocean Model, Journal of Advances in Modeling Earth Systems, 12, e2019MS001 904, https://doi.org/10.1029/2019MS001904, 2020.

Bachman, S. D., Fox-Kemper, B., Taylor, J. R., and Thomas, L. N.: Parameterization of frontal symmetric instabilities. I: Theory for resolved fronts, Ocean Modelling, 109, 72–95, https://doi.org/10.1016/j.ocemod.2016.12.003, 2017b.

Bischoff, T. and Thompson, A.: Configuration of a Southern Ocean Storm Track, Journal of Physical Oceanography, 44, 3072–3078, https://doi.org/10.1175/JPO-D-14-0062.1, 2014.

Blumen, W.: Uniform potential vorticity flow: Part I. Theory of wave interactions and two-dimensional turbulence, Journal of the Atmospheric Sciences, 35, 774–783, 1978.

Bolton, T. and Zanna, L.: Applications of Deep Learning to Ocean Data Inference and Subgrid Parameterization, Journal of Advances in Modeling Earth Systems, 11, 376–399, https://doi.org/10.1029/2018MS001472, 2019.

Boyd, J. P.: The Energy Spectrum of Fronts: Time Evolution of Shocks in Burgers ,Equation, Journal of Atmospheric Sciences, 49, 128–139, 1992.

Busecke, J. J. and Abernathey, R. P.: Ocean mesoscale mixing linked to climate variability, Science Advances, 5, 5014, https://doi.org/10.1126/sciadv.aav5014, 2019.

Callies, J. and Ferrari, R.: Interpreting energy and tracer spectra of upper-ocean turbulence in the submesoscale range (1-200 km), Journal of Physical Oceanography, 43, 2456–2474, https://doi.org/10.1175/JPO-D-13-063.1, 2013.

https://doi.org/10.5194/gmd-2024-72
Preprint. Discussion started: 29 April 2024

Geoscientific Model Development
Discussions

Cessi, P.: An Energy-Constrained Parameterization of Eddy Buoyancy Flux, Journal of Physical Oceanography, 38, 1807–1819, https://doi.org/10.1175/2007JPO3812.1, 2007.

Chapman, C. C., Lea, M.-A., Meyer, A., Sallée, J.-B., and Hindell, M.: Defining Southern Ocean fronts and their influence on biological and physical processes in a changing climate, Nature Climate Change, 10, 209–219, https://doi.org/10.1038/s41558-020-0705-4, 2020.

Charney, J. G.: Geostrophic turbulence, Journal of the Atmospheric Sciences, 28, 1087–1095, 1971.

Chelton, D., Deszoeke, R., Schlax, M. G., Naggar, K., and Siwertz, N.: Geographical Variability of the First Baroclinic Rossby Radius of Deformation, J. Phys. Oceanogr, 28, 433–460, https://doi.org/10.1175/1520-0485(1998)028<0433:GVOTFB>2.0.CO;2, 1998.

Chelton, D. B., Schlax, M. G., and Samelson, R. M.: Global observations of nonlinear mesoscale eddies, Progress in oceanography, 91, 167–216, https://doi.org/10.1016/j.pocean.2011.01.002, 2011.

Chen, C., Kamenkovich, I., and Berloff, P.: On the dynamics of flows induced by topographic ridges, Journal of Physical Oceanography, 45, 927–940, https://doi.org/10.1175/JPO-D-14-0143.1, 2015.

Cunningham, S. A., Alderson, S. G., King, B. A., and Brandon, M. A.: Transport and variability of the Antarctic circumpolar current in drake passage, Journal of Geophysical Research: Oceans, 108, https://doi.org/10.1029/2001JC001147, 2003.

Dong, C., McWilliams, J. C., Liu, Y., and Chen, D.: Global heat and salt transports by eddy movement, Nature communications, 5, 3294, https://doi.org/10.1038/ncomms4294, 2014.

Donohue, K. A., Tracey, K. L., Watts, D. R., Chidichimo, M. P., and Chereskin, T. K.: Mean Antarctic Circumpolar Current transport measured in Drake Passage, Geophysical Research Letters, 43, 11 760–11 767, https://doi.org/10.1002/2016GL070319, 2016.

Ferrari, R. and Wunsch, C.: Ocean circulation kinetic energy: Reservoirs, sources, and sinks, Annual Review of Fluid Mechanics, 41, 253–282, https://doi.org/10.1146/annurev.fluid.40.111406.102139, 2009.

Fox-Kemper, B. and Ferrari, R.: Parameterization of mixed layer eddies. Part II: Prognosis and impact, Journal of Physical Oceanography, 38, 1166–1179, https://doi.org/10.1175/2007JPO3788.1, 2008.

Fox-Kemper, B. and Menemenlis, D.: Can large eddy simulation techniques improve mesoscale rich ocean models?, Washington DC American Geophysical Union Geophysical Monograph Series, 177, 319–337, 2008.

Frezat, H., Le Sommer, J., Fablet, R., Balarac, G., and Lguensat, R.: A posteriori learning for quasi-geostrophic turbulence parametrization, Journal of Advances in Modeling Earth Systems, 14, e2022MS003 124, https://doi.org/10.1029/2022MS003124, 2022.

Fu, L.-L. and Morrow, R.: Remote sensing of the global ocean circulation, in: International Geophysics, vol. 103, pp. 83–111, Elsevier, 2013.

Gent and McWilliams, J.: Isopycnal Mixing in Ocean Circulation Models, Journal of Physical Oceanography, 20, 150–155, https://doi.org/10.1175/1520-0485(1990)020<0150:IMIOCM>2.0.CO;2, 1990.

Gent, P., McDougall, T., and McWilliams, J.: Parameterizing Eddy-Induced Tracer Transports in Ocean Circulation Models, J.phys.oceanogr, 25, 463–474, https://doi.org/10.1175/1520-0485(1995)025<0463:PEITTI>2.0.CO;2, 1995.

Germano, M.: Turbulence-The filtering approach, Journal of Fluid Mechanics, 238, https://doi.org/10.1017/S0022112092001733, 1992.

Germano, M., Piomelli, U., Moin, P., and Cabot, W.: A dynamic subgrid-scale eddy viscosity model, Physics of Fluids, 3, 1760–1765, https://doi.org/10.1063/1.857955, 1991.

Graham, J. and Ringler, T.: A framework for the evaluation of turbulence closures used in mesoscale ocean large-eddy simulations, Ocean Modelling, 65, 25–39, https://doi.org/10.1016/j.ocemod.2013.01.004, 2013.

Griffies, S., Gnanadesikan, A., Pacanowski, R., Larichev, V., and Smith, R.: Isoneutral Diffusion in a z-Coordinate Ocean Model, J.phys.oceanogr, 28, 805–830, https://doi.org/10.1175/1520-0485(1998)028<0805:IDIAZC>2.0.CO;2, 1998.

Guillaumin, A. P. and Zanna, L.: Stochastic-deep learning parameterization of ocean momentum forcing, Journal of Advances in Modeling Earth Systems, 13, e2021MS002 534, https://doi.org/10.1029/2021MS002534, 2021.

Gula, J., Molemaker, M. J., and McWilliams, J. C.: Submesoscale cold filaments in the Gulf Stream, Journal of Physical Oceanography, 44, 2617–2643, https://doi.org/10.1175/JPO-D-14-0029.1, 2014.

Haigh, M. and Berloff, P.: On co-existing diffusive and anti-diffusive tracer transport by oceanic mesoscale eddies, Ocean Modelling, 168, 101 909, https://doi.org/10.1016/j.ocemod.2021.101909, 2021.

Hallberg, R.: Using a resolution function to regulate parameterizations of oceanic mesoscale eddy effects, Ocean Modelling, 72, 92–103, https://doi.org/10.1016/j.ocemod.2013.08.007, 2013.

Held, I. M., Pierrehumbert, R. T., Garner, S. T., and Swanson, K. L.: Surface quasi-geostrophic dynamics, Journal of Fluid Mechanics, 282, 1–20, 1995.

Jansen, M. F. and Held, I. M.: Parameterizing subgrid-scale eddy effects using energetically consistent backscatter, Ocean Modelling, 80, 36–48, https://doi.org/10.1016/j.ocemod.2014.06.002, 2014.

Jansen, M. F., Adcroft, A., Khani, S., and Kong, H.: Toward an energetically consistent, resolution aware parameterization of ocean mesoscale eddies, Journal of Advances in Modeling Earth Systems, 11, 2844–2860, https://doi.org/10.1029/2019MS001750, 2019.

Kaneda, Y. and Ishihara, T.: High-resolution direct numerical simulation of turbulence, Journal of Turbulence, p. N20, https://doi.org/https://doi.org/10.1080/14685240500256099, 2006.

Khani, S. and Dawson, C. N.: A Gradient Based Subgrid-Scale Parameterization for Ocean Mesoscale Eddies, Journal of Advances in Modeling Earth Systems, 15, e2022MS003 356, https://doi.org/10.1029/2022MS003356, 2023.

Khani, S., Jansen, M., and Adcroft, A.: Diagnosing Subgrid Mesoscale Eddy Fluxes With and Without Topography, Journal of Advances in Modeling Earth Systems, 11, 3995–4015, https://doi.org/10.1029/2019MS001721, 2019.

Khatri, H. and Berloff, P.: A mechanism for jet drift over topography, Journal of Fluid Mechanics, 845, 392–416, https://doi.org/10.1017/jfm.2018.260, 2018.

LaCasce, J. H. and Groeskamp, S.: Baroclinic modes over rough bathymetry and the surface deformation radius, Journal of Physical Oceanography, 50, 2835–2847, https://doi.org/10.1175/JPO-D-20-0055.1, 2020.

Lapeyre, G.: Surface quasi-geostrophy, Fluids, 2, 7, 2017.

Leonard, A.: Energy cascade in large-eddy simulations of turbulent fluid flows, in: Turbulent Diffusion in Environmental Pollution, 1974.

Lu, J. and Speer, K.: Topography, jets, and eddy mixing in the Southern Ocean, Journal of Marine Research, 68, 479–502, https://doi.org/10.1357/002224010794657227, 2010.

Lutjeharms, J. and Van Ballegooyen, R.: Topographic control in the Agulhas Current system, Deep Sea Research, 31, 1321–1337, 1984.

Lutjeharms, J. R. E.: Three decades of research on the greater Agulhas Current, Ocean Science, 3, 129–147, https://doi.org/10.5194/os-3-129-2007, 2007.

Ma, X., Jing, Z., Chang, P., Liu, X., Montuoro, R., Small, R. J., Bryan, F. O., Greatbatch, R. J., Brandt, P., Wu, D., et al.: Western boundary currents regulated by interaction between ocean eddies and the atmosphere, Nature, 535, 533–537, https://doi.org/10.1038/nature18640, 2016.

Mak, J., Maddison, J. R., Marshall, D. P., and Munday, D. R.: Implementation of a geometrically informed and energetically constrained mesoscale eddy parameterization in an ocean circulation model, Journal of Physical Oceanography, 48, 2363–2382, https://doi.org/10.1175/JPO-D-18-0017.1, 2018.

Marques, G., Loose, N., Yankovsky, E., Steinberg, J., Chang, C., Bhamidipati, N., Adcroft, A., Fox-Kemper, B., Griffies, S., Hallberg, R., Jansen, M., Khatri, H., and Zanna, L.: NeverWorld2: an idealized model hierarchy to investigate ocean mesoscale eddies across resolutions, Geoscientific Model Development, 15, 6567–6579, https://doi.org/10.5194/gmd-15-6567-2022, 2022.

Marshall, J., Adcroft, A., Hill, C., Perelman, L., and Heisey, C.: A finite-volume, incompressible Navier-Stokes model for studies of the ocean on parallel computers, Journal of Geophysical Research: Oceans, 102, https://doi.org/10.1029/96JC02775, 1997.

Mazloff, M., Heimbach, P., and Wunsch, C.: An Eddy-Permitting Southern Ocean State Estimate, Journal of Physical Oceanography, 40, 880–899, https://doi.org/10.1175/2009JPO4236.1, 2010.

McWilliams, J.: Submesoscale currents in the ocean, Proceedings of the Royal Society A: Mathematical, Physical and Engineering Sciences, 472, 0117, https://doi.org/10.1098/rspa.2016.0117, 2016.

Meneveau, C.: Statistics of turbulence subgrid-scale stresses: Necessary conditions and experimental tests, Physics of Fluids, 6, 815–833, https://doi.org/10.1063/1.868320, 1994.

Moin, P. and Mahesh, K.: Direct numerical simulation: a tool in turbulence research, Annual review of fluid mechanics, 30, 539–578, https://doi.org/https://doi.org/10.1146/annurev.fluid.30.1.539, 1998.

Moser, R., Haering, S., and Yalla, G.: Statistical Properties of Subgrid-Scale Turbulence Models, Annual Review of Fluid Mechanics, 53, https://doi.org/10.1146/annurev-fluid-060420-023735, 2021.

Orsi, A. H., Whitworth III, T., and Nowlin Jr, W. D.: On the meridional extent and fronts of the Antarctic Circumpolar Current, Deep Sea Research Part I: Oceanographic Research Papers, 42, 641–673, https://doi.org/10.1016/0967-0637(95)00021-W, 1995.

Park, Y.-h., Vivier, F., Roquet, F., and Kestenare, E.: Direct observations of the ACC transport across the Kerguelen Plateau, Geophysical Research Letters, 36, https://doi.org/10.1029/2009GL039617, 2009.

Pearson, B., Fox-Kemper, B., Bachman, S., and Bryan, F.: Evaluation of scale-aware subgrid mesoscale eddy models in a global eddy-rich model, Ocean Modelling, 115, 42–58, https://doi.org/10.1016/j.ocemod.2017.05.007, 2017.

Perezhogin, P. and Glazunov, A.: Subgrid parameterizations of ocean mesoscale eddies based on Germano decomposition, Journal of Advances in Modeling Earth Systems, 15, e2023MS003 771, https://doi.org/10.1029/2023MS003771, 2023.

Pope, S.: Turbulent Flows, Cambridge University Press, 2000.

Radko, T. and Kamenkovich, I.: On the topographic modulation of large-scale eddying flows, Journal of Physical Oceanography, 47, 2157–2172, https://doi.org/10.1175/JPO-D-17-0024.1, 2017.

Redi, M.: Oceanic Isopycnal Mixing by Coordinate Rotation, Journal of Physical Oceanography, 12, 1154–1158, https://doi.org/10.1175/1520-0485(1982)012<1154:OIMBCR>2.0.CO;2, 1982.

Rhines, P. B.: Jets and Orography: Idealized Experiments with Tip Jets and Lighthill Blocking, Journal of the Atmosphericences, 64, 3627, https://doi.org/10.1175/JAS4008.1, 2006.

Schubert, R., Schwarzkopf, F. U., Baschek, B., and Biastoch, A.: Submesoscale impacts on mesoscale Agulhas dynamics, Journal of Advances in Modeling Earth Systems, 11, 2745–2767, https://doi.org/10.1029/2019MS001724, 2019.

Schubert, R., Gula, J., Greatbatch, R. J., Baschek, B., and Biastoch, A.: The submesoscale kinetic energy cascade: Mesoscale absorption of submesoscale mixed layer eddies and frontal downscale fluxes, Journal of Physical Oceanography, 50, 2573–2589, https://doi.org/10.1175/JPO-D-19-0311.1, 2020.

Siedler, G., Griffies, S., and Church, J.: Ocean circulation and climate: a 21st century perspective, Academic Press, 2013.

Smith, R. and Gent, P.: Anisotropic Gent-McWilliams Parameterization for Ocean Models, Journal of Physical Oceanography, 34, 2541, https://doi.org/10.1175/JPO2613.1, 2004.

https://doi.org/10.5194/gmd-2024-72
Preprint. Discussion started: 29 April 2024

Speich, S., Lutjeharms, J. R. E., Penven, P., and Blanke, B.: Role of bathymetry in Agulhas Current configuration and behaviour, Geophysical Research Letters, 33, https://doi.org/10.1029/2006GL027157, 2006.

Stammer, D.: On eddy characteristics, eddy transports, and mean flow properties, Journal of Physical Oceanography, 28, 727–739, https://doi.org/10.1175/1520-0485(1998)028<0727:OECETA>2.0.CO;2, 1998.

Taylor, J. R. and Thompson, A. F.: Submesoscale dynamics in the upper ocean, Annual Review of Fluid Mechanics, 55, 103–127, https://doi.org/10.1146/annurev-fluid-031422-095147, 2023.

Thomas, L. N., Tandon, A., and Mahadevan, A.: Submesoscale Processes and Dynamics, Ocean Modeling in an Eddying Regime, 177, 17–38, 2008.

Thompson: Jet Formation and Evolution in Baroclinic Turbulence with Simple Topography, J.phys.oceanogr, 40, 257–278, https://doi.org/10.1175/2009JPO4218.1, 2010.

Thompson and Naveira-Garabato, A.: Equilibration of the Antarctic Circumpolar Current by Standing Meanders, Journal of Physical Oceanography, 44, 1811–1828, https://doi.org/10.1175/JPO-D-13-0163.1, 2014.

Thompson and Sallee, J.: Jets and Topography: Jet Transitions and the Impact on Transport in the Antarctic Circumpolar Current, Journal of Physical Oceanography, 42, 956–972, https://doi.org/10.1175/JPO-D-11-0135.1, 2012.

Vallis, G.: Atmospheric and oceanic fluid dynamics, 2017.

Verdy, A. and Mazloff, M.: A data assimilating model for estimating Southern Ocean biogeochemistry, Journal of Geophysical Research: Oceans, 122, 6968–6988, https://doi.org/10.1002/2016JC012650, 2017.

Visbeck, M., Marshall, J., Haine, T., and Spall, M.: Specification of Eddy Transfer Coefficients in Coarse-Resolution Ocean Circulation Models, Journal of Physical Oceanography, 27, 381–402, https://doi.org/10.1175/1520-0485(1997)027<0381:SOETCI>2.0.CO;2, 1997.

Wei, H. and Wang, Y.: Full-depth scalings for isopycnal eddy mixing across continental slopes under upwelling-favorable winds, Journal of Advances in Modeling Earth Systems, 13, https://doi.org/10.1029/2021MS002498, 2021.

Xie, J., Liu, H., and Lin, P.: A multifaceted isoneutral eddy transport diagnostic framework and its application in the Southern Ocean, Journal of Advances in Modeling Earth Systems, 15, e2023MS003 728, https://doi.org/10.1029/2023MS003728, 2023.

Xu, X., Chassignet, E. P., Firing, Y. L., and Donohue, K.: Antarctic Circumpolar Current Transport Through Drake Passage: What Can We Learn From Comparing High-Resolution Model Results to Observations?, Journal of Geophysical Research: Oceans, 125, https://doi.org/10.1029/2020JC016365, 2020.

Yankovsky, E., Legg, S., and Hallberg, R.: Parameterization of submesoscale symmetric instability in dense flows along topography, Journal of Advances in Modeling Earth Systems, 13, e2020MS002 264, https://doi.org/10.1029/2020MS002264, 2021.

Youngs, M., Thompson, A., Lazar, A., and Richards, K.: ACC Meanders, Energy Transfer, and Mixed Barotropic-Baroclinic Instability, Journal of Physical Oceanography, 47, 1291–1305, https://doi.org/10.1175/JPO-D-16-0160.1, 2017.

Zanna, L. and Bolton, T.: Data-driven equation discovery of ocean mesoscale closures, Geophysical Research Letters, 47, e2020GL088 376, https://doi.org/10.1029/2020GL088376, 2020.

Zhai, X., Johnson, H. L., and Marshall, D. P.: Significant sink of ocean-eddy energy near western boundaries, Nature Geoscience, 3, 608–612, https://doi.org/10.1038/NGEO943, 2010.

Zhang, J., Zhang, Z., and Qiu, B.: Parameterizing Submesoscale Vertical Buoyancy Flux by Simultaneously Considering Baroclinic Instability and Strain-Induced Frontogenesis, Geophysical Research Letters, 50, e2022GL102 292, https://doi.org/10.1029/2022GL102292, 2023.